Article: Retrieval of aerosol profiles combining sunphotometer and ceilometer measurements in GRASP code.

Authors: R. Román, J.A. Benavent-Oltra, J.A. Casquero-Vera, A. Lopatin, A. Cazorla, H. Lyamani, C. Denjean, D. Fuertes, D. Pérez-Ramírez, B. Torres, C. Toledano, O. Dubovik, V.E. Cachorro, A.M. de Frutos, F.J. Olmo, and L. Alados-Arboledas

Journal: Atmospheric Research

Volume: 204

Pages: 161-177

Year: 2018

DOI: 10.1016/j.atmosres.2018.01.021

Retrieval of aerosol profiles combining sunphotometer and ceilometer measurements in GRASP code

R. Román[1,2,3], J.A. Benavent-Oltra[1,3], J.A. Casquero-Vera[1,3], A. Lopatin[4], A. Cazorla[1,3], H. Lyamani[1,3], C. Denjean[5], D. Fuertes[4], D. Pérez-Ramírez[1,3], B. Torres[4], C. Toledano[2], O. Dubovik[4,6], V.E. Cachorro[2], A.M. de Frutos[2], F.J. Olmo[1,3], and L. Alados-Arboledas[1,3]

[1]{Department of Applied Physics, University of Granada. 18071, Granada (Spain)}

[2]{Grupo de Óptica Atmosférica (GOA), Universidad de Valladolid. Paseo Belén, 7, 47011, Valladolid (Spain)}

[3]{Andalusian Institute for Earth System Research (IISTA-CEAMA), University of Granada, Autonomous Government of Andalusia. 18006, Granada (Spain)}

[4]{GRASP-SAS, Remote sensing developments, LOA / Université Lille-1, Villeneuve d'Ascq, France}

[5]{CNRM, Centre National de la Recherche Météorologique (UMR3589, CNRS, Météo-France), Toulouse, France}

[6]{Laboratoire d'Optique Atmosphérique, Université de Lille 1, Villeneuve d'Ascq, France}

Abstract

In this paper we present an approach for the profiling of aerosol microphysical and optical properties combining ceilometer and sun/sky photometer measurements in the GRASP code (General Retrieval of Aerosol and Surface Properties). For this objective, GRASP is used with sun/sky photometer measurements of aerosol optical depth (AOD) and sky radiances, both at four wavelengths and obtained from AErosol RObotic NETwork (AERONET), and ceilometer measurements of range corrected signal (RCS) at 1064 nm. A sensitivity study with synthetic data evidences the capability of the method to retrieve aerosol properties such as size distribution and profiles of volume concentration (VC), especially for coarse particles. Aerosol properties obtained by the mentioned method are compared with airborne in-situ measurements acquired during two flights over Granada (Spain) within the framework of ChArMEx/ADRIMED (Chemistry-Aerosol Mediterranean Experiment/Aerosol Direct Radiative Impact on the regional climate in the MEDiterranean region) 2013 campaign. The retrieved aerosol VC profiles agree well with the airborne measurements, showing a mean bias error (MBE) and a mean absolute bias error (MABE) of 0.3 $\mu m^3/cm^3$ (12%) and 5.8 $\mu m^3/cm^3$ (25%), respectively. The differences between retrieved VC and airborne in-situ measurements are within the uncertainty of GRASP retrievals. In addition, the retrieved VC at 2500 m a.s.l. is shown and compared with in-situ measurements obtained during summer 2016 at a high-atitude mountain station in the framework of the SLOPE I campaign (Sierra Nevada Lidar AerOsol Profiling Experiment). VC from GRASP presents high correlation (r=0.91) with the in-situ measurements, but overestimates them, MBE and MABE being equal to 23% and 43%.

Keywords

GRASP, ceilometer, aerosol, profiling, photometer, aerosol volume concentration.

1 Introduction

Aerosols are a key piece in the Earth climatic system because they can increase the cooling or warming of the Earth surface depending on their properties (Boucher et al., 2013). Hence, columnar and vertical aerosol properties must be appropriately known to better understand their impact in the Earth energy balance and therefore on the Earth climate. Furthermore aerosol profiling is also relevant in the management of aviation traffic (Prata, 2009; Flentje et al., 2010).

Column-integrated microphysical and optical aerosol properties are commonly retrieved by sun/sky photometer measurements. This is the case of AERONET (AErosol RObotic NETwork; Holben et al., 1998), that derives aerosol optical depth (AOD) from multiwavelength measurements of direct beam sun irradiance, and uses these AOD values in combination with sky radiances measurements for obtaining aerosol properties such as aerosol size distribution, refractive indices, single scattering albedo (SSA), and phase function (Dubovik and King, 2000; Dubovik et al., 2006). However, this kind of measurements does not provide information about the vertical profile of these aerosol properties.

Lidar systems are capable of measuring the atmospheric backscatter profile at several wavelengths. The lidar signals are used for profiling optical and even retrieving microphysical aerosol properties applying different methods. These methods depend on the available lidar signals: elastic range corrected signal (RCS) is useful to provide aerosol backscatter (β) profiles (Klett, 1981, 1985; Fernald, 1984; Sasano, 1984); non-elastic (Raman) signal can be used for obtaining independent range-resolved extinction (α) and backscatter coefficients (Ansmann et al., 1990; Whiteman et al., 1992). Elastic and Raman lidar signals can be combined, usually by the so called $3\beta+2\alpha$ configuration, to obtain profiles of aerosol microphysical properties through different inversion techniques (e.g. Müller et al., 1999; Böckmann, 2001; Veselovskii et al., 2002, 2012; Chemyakin et al., 2016).; many papers being already published for characterizing long-transport of biomass-burning (e.g. Veselovskii et al., 2015; Ortiz-Amezcua et al., 2017), volcanic aerosol (e.g. Navas-Guzmán et al., 2013), dust (e.g. Granados-Muñoz et al., 2016; Veselovskii et al., 2017) pollution (e.g. Wandinger et al., 2002; Noh et al., 2009; Veselovskii et al., 2013), and artic haze (Müller et al., 2004). In addition, linear particle depolarization ratio measurements allow the detection and assessment of non-spherical particles such as dust or volcanic aerosol (e.g. Ansmann et al., 2009, 2012; Tesche et al., 2009, 2011; Bravo-Aranda et al., 2013) and allows aerosol typing (e.g. Burton et al., 2012; Gross et al., 2013).

EARLINET (European Aerosol Research LIdar NETwork; Pappalardo et al., 2014), founded in 2000 and now part of ACTRIS (Aerosols, Clouds, and Trace gases Research InfraStructure ; www.actris.eu/), does include nowadays 31 lidar stations, most of them operating multiwavelength Raman lidars. However, most Raman measurements are sparse and mostly limited to night-time. To retrieve vertical profiles of aerosol microphysics, several inversion techniques were developed within EARLINET/ACTRIS combining backscattering lidar and collocated AERONET sun/sky photometers such as LIRIC (Lidar Radiometer Inversion Code; Chaikovsky et al., 2008, 2016) and GARRLiC (Generalized Aerosol Retrieval from Radiometer and Lidar Combined data; Lopatin et al., 2013). The LIRIC code uses AERONET column-integrated retrievals plus backscattering lidar signals as inputs to provide vertical-resolved aerosol volume concentration (VC), both at fine and coarse mode. However, GARRLiC uses as inputs measured optical depth and sky radiances and the multiwavelength RCS from lidar to provide vertical-resolved aerosol microphysical and optical properties, both at fine and coarse mode, and also improves the classical

AERONET columnar retrievals by providing intensive aerosol properties, like refractive indices or SSA, of fine and coarse modes, separately.

The Generalized Retrieval of Aerosol and Surface Properties (GRASP; Dubovik et al., 2014) code uses the heritage of AERONET inversion scheme (e.g. Dubovik and King, 2000; Dubovik et al., 2006) and is a versatile and open-source algorithm capable to obtain optical and microphysical aerosol properties from different sources of measurements (www.grasp-open.com). Recently, aerosol properties have been retrieved by GRASP using, among other information sources, satellite images (Kokhanovsky et al., 2015), polar nephelometer data (Espinosa et al., 2017) and different combinations with sun/sky photometer measurements: only spectral AODs (Torres et al., 2017); spectral AODs, sky radiances and polarized sky radiances (Fedarenka et al., 2016); and spectral AODs and sky camera images (Román et al., 2017a). The incorporation of the GARRLiC scheme in GRASP allows to combine AODs, sky radiances and RCS lidar values to retrieve columnar and vertical-resolved aerosol properties discerning between fine and coarse modes (Lopatin et al., 2013; Bovchaliuk et al., 2016; Benavent-Oltra et al., 2017).

Although the combination of lidar and sun/sky photometer measurements using GRASP with the GARRLiC scheme is promising, lidar systems are generally expensive and require supervision, so few stations have the set of measurements required to this end. An alternative to multiwavelength lidar systems could be the use of ceilometers, which were originally designed for studying cloud heights but recent ceilometer models are able to detect aerosol layers at altitudes of up to 10 km. Ceilometers only measure at one wavelength and are less accurate than classic lidars, but they are cheaper and more operative than multiwavelength lidar systems and they also can work continuously unattended. In fact, ceilometers have been previously used to obtain aerosol properties as PM2.5 (Li et al., 2017), PM10 (Münkel et al., 2007), aerosol backscatter coefficients (Heese et al., 2010; Wiegner and Geiss, 2012; Wiegner et al., 2014; Madonna et al., 2015) or aerosol hygroscopic growth (Haeffelin et al., 2016). Moreover, there are some programs nowadays as E-PROFILE, a program of EUMETNET (EUropean METeorological services NETwork), and the COST Action ES1303 TOPROF (TOwards operational ground based PROFiling with ceilometers, doppler lidars and microwave radiometers for improving weather forecasts) dealing with the harmonization and better characterization of ceilometer measurements and products; and there are also ceilometer networks, like the Iberian CEilometer NETwork (ICENET; Cazorla et al., 2017) among others (e.g., de Haij et al., 2007; Emeis et al., 2011), trying to provide ceilometer measurements in near-real time with devices every 100 km. These issues motivate to try to combine ceilometer measurements with sun/sky photometer in order to obtain some vertical aerosol information.

The main objective of this work is use for the first time the GRASP code to obtain aerosol vertical profiling of aerosol microphyscial properties combining AERONET sun/sky photometer measurements with the monochromatic RCS measured by a ceilometer at 1064 nm. The use of this proposed combination of measurements allows the retrievals of column-integrated aerosol microphysical properties, and we explore the possibility of obtaining vertically-resolved aerosol volume concentration. Another important goal is the quantification of the accuracy and uncertainty of all retrieved parameters through synthetic data and also by comparisons of retrieved parameters versus in-situ measurements

This paper is structured as follows: Section 2 describes the used instrumentation during the different measurement field campaigns; Section 3 introduces the GRASP code and the methodology to retrieve the aerosol properties; a sensitivity study with synthetic measurements is developed in Section 4 in order to test the capability of the proposed GRASP scheme. Section 5 shows the main results about the comparison of the obtained aerosol retrievals against in-situ measurements and, finally, the main conclusions are summarized in Section 6.

2 Instrumentation and campaigns

2.1 Instrumentation at Granada station

Most of the instrumentation used in this work is installed on the rooftop of the "Andalusian Institute for Earth System Research" (IISTA-CEAMA) building at Granada, Spain (37.1638º N; 3.6051º W; 680 m a.s.l.). This instrumentation is managed by the Atmospheric Physics Group ("Grupo de Física de la Atmósfera"; GFAT) of University of Granada. Granada is a Spanish city located in the South-Eastern of the Iberian Peninsula, in a natural basin surrounded by –Sierra Nevada Mountains with peaks of up to 3300 m a.s.l., showing a Mediterranean climate (Csa in Köppen classification). The city is medium-size with a population about 235000 inhabitants, which increases up to 530000 including the metropolitan area, and non-industrialized being its main aerosol sources the domestic heating based on fuel oil combustion in winter and the heavy traffic along all year (Lyamani et al., 2010, 2011; Titos et al., 2012, 2014). Columnar aerosol pattern in the area is characterized by higher values in summer mostly associated with Saharan dust arrivals (Pérez-Ramírez et al., 2012; Mandija et al., 2016), while the lowest aerosol loads usually corresponds to the arrivals of Atlantic air-masses that clean the atmosphere (Pérez-Ramírez et al., 2016).

A CE318-T sun/sky/lunar (triple) photometer (*Cimel Electronique*) is operative on the mentioned station since March 2016 for providing day and night columnar aerosol optical properties (Barreto et al., 2013, 2016). GFAT also operates different sun/sky photometers (hereafter 'sunphotometers') which belong to AERONET and have participated in field campaigns in Spain, Brazil, Colombia and Bolivia, and have allowed continuous operation of the site in Granada since the end of 2004. Both sunphotometer models take measurements of direct beam sun irradiance, which retrieve AOD, and sky radiance at several wavelengths, but only the channels of 440, 675, 870 and 1020 nm are chosen in this work because they are available in most AERONET sunphotometers. All sunphotometer data used have been obtained from version 2 of AERONET as level 1.5 data. Level 1.5 data are cloud-screened and have been chosen instead of quality assurance level 2.0 data due to the near-real time availability of these data, which can be used to calculate also other products in near-real time.

The mentioned Granada station also includes a "CHM-15k Nimbus" ceilometer (*Lufft manufacturer*), which belongs to ICENET (Cazorla et al., 2017) and is detailed in Román et al. (2017b). This instrument works as a one-wavelength lidar which emits at 1064 nm (a pulsed Nd:YAG laser) and measures the backscattered signal by the atmosphere at different heights (up to 15360 m a.g.l.) with 15 m resolution. According to the overlap function provided by the manufacturer, the overlap is 90% complete between 555 and 885 m a.g.l. (Cazorla et al., 2017). The firmware of the instrument directly provides NetCDF files with the RCS at 1064 nm which includes background and overlap corrections. In addition, these files include the cloud base height (CBH) product, which is estimated from ceilometer measurements due to the strong backscattered signal of clouds (Martucci et al., 2010). The data are recorded as time averaged data every 15 seconds. More information about this ceilometer and its products can be found in the Jenoptik CHM15k user manual (Jenoptik, 2013).

2.2 ChArMEx/ADRIMED 2013

One of the main objectives of the ChArMEx/ADRIMED campaign (Chemistry-Aerosol Mediterranean Experiment/Aerosol Direct Radiative Impact on the regional climate in the MEDiterranean region) during summer 2013 was to conduct an experimental campaign, based on surface and aircraft observations, for creating a rich 3-D database of physical, chemical and optical properties of the main Mediterranean aerosols (Mallet et al., 2016). To this end, 16 flights, ascending or descending in a spiral trajectory during 30 min, were performed over the Mediterranean Basin with the ATR-42 aircraft of SAFIRE (French aircraft service for environmental research; http://www.safire.fr) during the period from 14th June to 4th July 2013 (Mallet et al. 2016; Denjean et al., 2016). The two flights named F30 and F31 of this campaign were done over Granada city on 16th and 17th June 2013, respectively.

In both flights the ATR-42 airplane was equipped with different in-situ instrumentation, being used in this work the measurements of fine and coarse aerosol concentrations. For the aerosol concentration measurements in the submicron range: an UHSAS (Ultra-High Sensitivity Aerosol Spectrometer; *Droplet Measurement Technologies*) and a SMPS (Scanning Mobility Particle Sizer) with an accuracy of 10% (Cai et al., 2008) and 5% (Wiedensohler et al., 2012), respectively. For coarse particles the optical size distributions was measured by a FSSP-300 (a wing-mounted Forward Scattering Spectrometer Probe, model 300 from *Particle Measuring Systems*) and by the in-cabin GRIMM OPC (sky-optical particle counter; model 1.129 from *Grimm Technik*) in the diameter nominal size ranges of 0.28-20 µm and 0.25-32 µm, respectively. FSSP-300 and GRIMM have an accuracy of 30% (Baumgardner et al., 1992) and 10% (Denjean et al., 2016), respectively. Finally, the profiles of the total aerosol VC (for radius ranging between 0.05 and 15 µm) have been obtained with a resolution of 100 m as in Benavent-Oltra et al. (2017): combining all the measurements of aerosol number size distributions (SMPS, UHSAS, FSSP-300 and GRIMM OPC) and assuming that aerosol particles are spherical (Denjean et al., 2016).

2.3 SLOPE I

The SLOPE I campaign (Sierra Nevada Lidar AerOsol Profiling Experiment) was designed in order to measure relevant data for testing different retrieval schemes of aerosol microphysical and optical vertical-profiles from remote sensing observations. The campaign, developed during summer 2016, combined active and passive remote sensing of the vertical column with in-situ measurements at several levels in the northwestern slope of Sierra Nevada mountain range (Spain). In this framework, a new measurement (SNS: Sierra Nevada Station) was set up in a high-altitude site at Sierra Nevada (37.0958º N; 3.3869º W; 2500 m a.s.l.). This new station is 20 km far from IISTA-CEAMA in horizontal distance and it was equipped with aerosol in-situ instrumentation since May 2016, providing 24-hour aerosol in-situ measurements such as scattering, absorption and extinction coefficients.

The in-situ aerosol volume concentration at SNS has been calculated combining SMPS (model 3938 from *TSI Inc.*) and APS (Aerodynamic Particle Sizer; model 3321 from *TSI Inc.*) measurements. This volume concentration has been obtained in the 0.05-10 µm radius range with 5 minutes time resolution. For that, Q-value = 1 is assumed for conversion from aerodynamic (APS) to mobility size distribution (Sorribas et al., 2015).

3 GRASP retrieval

3.1 Inputs

3.1.1 Sun/sky photometer data

CE318 sunphotometers are configured to take a sequence of sky radiance measurements in the almucantar plane (zenith angle equal to solar zenith angle, SZA) for several air masses. AERONET provides the sky radiance usually at the next almucantar azimuth angles (relative to sun): 2º, 2.5º, 3º, 3.5º, 4º, 5º, 6º, 7º, 8º, 10º, 12º, 14º, 16º, 18º, 20º, 25º, 30º, 35º, 40º, 45º, 50º, 60º, 70º, 80º, 90º, 100º, 120º, 140º, 160º and 180º. These angles are scanned clockwise and counter clockwise giving two measurements for each angle of symmetric points with respect to the sun position. In this work the sky radiance has been averaged between both points. The azimuth angles below 3.5º are rejected following the same criteria than the version 1 level 1.5 of AERONET (Holben et al., 2006). The angles showing differences above 20% between both almucantar branches are assumed as cloud contaminated and are also discarded as in level 1.5 of AERONET version 2 (Holben et al., 2006). The azimuth at 180º does not have a symmetric point which makes difficult its cloud-screening, and hence this angle is also rejected. These criteria provide, in the most favourable case, 26 sky radiance values at the four channels at 440 nm, 675 nm, 870 nm and 1020 nm.

After cloud-screening, the scattering angle criterion of Holben et al. (2006) for AERONET (version 2 level 1.5) is applied. This criterion considers that sky radiance distribution for each wavelength is representative if there is at least one measurement in four regions identified by the scattering angle: ≥3.2º to 6º; ≥6º to 30º; ≥30º to 80º; and ≥80º. In this work the scattering angle of 80º has been replaced in these bins by 78º in order to use almucantars with SZA up to 40º.

The GRASP retrievals are done for each available cloud-screened almucantar if it satisfies: (1) the number of sky radiance points at each wavelength is higher or equal than 10 (as in AERONET version 2 level 1.5); (2) at each wavelength there is at least one radiance value at the four mentioned bins, and (3) the closest AOD (level 1.5), also used in the retrieval, is within ±16 min of almucantar measurement for the four wavelengths. Sky radiance data used as input in GRASP is previously normalized using the "2000 ASTM Standard Extraterrestrial Spectrum Reference E-490-00" (http://rredc.nrel.gov/solar/spectra/am0), again the same than in AERONET version 2 aerosol inversions. In order to include the filter response of the photometer, the extraterrestrial spectrum is convoluted for each channel by a 10 nm width square filter (similar to the real filters) centred in the effective wavelength of the real photometer filters.

3.1.2 Ceilometer

For each almucantar dataset the correlative ceilometer RCS values measured without clouds (CBH provided by the instrument is null) are averaged in a ±15 min window centred around the almucantar time. A minimum of 5 RCS cloud-free profiles is imposed for calculating the average and for consequently running GRASP. This requirement of at least 5 profiles is not too restrictive working with averaged 15-seconds profiles and could provide averaged profiles too noisy when the number of used profiles in the averaging is closer to (and above) 5, but most of them will be only taken into account up to low altitudes due to the used iterative method to reject noisy points that is explained below; this threshold may be increased in future works, but now it permits to obtain more retrievals. The time averaged RCS is vertically smoothed by a moving average of ±105 m window in order to reduce noise, and later it is normalized at 60 log-spaced bins at different heights, as in Lopatin et al. (2013), being the minimum of these heights (z_{min}) equal to 250 m a.s.l. since the ceilometer shows frequently very noisy signal below this height due to the overlap correction. The maximum height (z_{max}) selected for the 60 log-spaced bins is 7000 m a.s.l. since aerosol layers are rarely detected above this height and the ceilometer signal is usually too noisy, due to the low power of ceilometer´s laser. The RCS at these 60 log-spaced bins is normalized by dividing the average of RCS in each logarithmic height interval by the integrated RCS between z_{min} and z_{max} according to the following equation:

$$NRCS_h = \frac{\frac{1}{N}\sum_{z=h_1}^{z=h_N} RCS_z}{\int_{z_{min}}^{z_{max}} RCS_z dz} \quad (1)$$

where $NRCS_h$ is the normalized RCS at the h-bin (h ranges from 1 to 60), N is the number of available RCS values in the height interval given by the h-bin, and h_1, h_2, ... and h_N represents the N heights of the available RCS that are inside the h-bin.

Due to the background correction and the noisy signal at high altitudes, the smooth and normalization process occasionally provides negative values of normalized RCS, which cannot be processed by GRASP due to the lack of physical sense. An iterative method has been applied to solve this issue: if any normalized RCS value is negative then the 60 log-spaced bins and normalized values are recalculated considering the maximum height 100 m below the last; this loop with z_{max} decreasing 100 m per iteration stops when all values of normalized RCS are positive.

3.1.3 BRDF data

A part of measured sky radiance has its source in the light reflected by the Earth surface; therefore, the Bidirectional Reflectance Distribution Function (BRDF) is used to take into account this phenomenon. The BRDF is introduced in GRASP through the BRDF parameters of the Li–Ross model (Ross, 1981; Li and Strahler, 1992). GRASP is capable to calculate BRDF parameters from satellite images (Dubovik et al., 2014) but the BRDF parameters used for this work are obtained from the V005 Collection MCD43C1 product (V005 MODIS Terra+Aqua BRDF/Albedo 16-Day L3 0.05Deg CMG) of MODIS (MODerate-resolution Imaging Spectroradiometer) with a spatial resolution of 0.05º (Schaff et al., 2011). This product is produced every 8 days with 16 days of acquisitions at seven narrow bands, which central wavelengths are 470, 555, 659, 858, 1240, 1640 and 2130 nm. The available MCD43C1 data at the Granada coordinates from 2000 to 2014 have been averaged obtaining a table of BRDF parameters every 8 days for one representative year. The BRDF parameters used in a particular GRASP retrieval are obtained from the mentioned table taken into account the date and linearly interpolating the central wavelengths of MCD43C1 product to 675, 870, 1020 and 1064 nm and extrapolating to 440 nm.

3.2 Inversion strategy, constraints and products

GRASP includes two independent modules, the first is the forward model based on radiative transfer and aerosol model, which is capable to generate the radiative measurements for a given aerosol scenario (Dubovik et al., 2014). This forward model is used in Section 4 to simulate synthetic data for different aerosol scenarios. The second module corresponds to the numerical inversion, which includes general mathematical operations, based on multi-term least square method (Dubovik and King, 2000), not related to the particular physical nature of the inverted data (Dubovik et al., 2014). This module, combined with the forward module, allows flexible and rigorous inversions of the various combinations of the independent multi-source measurements. Detailed description about how GRASP and its modules work using sunphotometer and RCS data was given by Lopatin et al. (2013), who explained the GARRLiC algorithm which nowadays is part of GRASP code.

The use of sunphotometer and ceilometer data proposed in this work cannot discern between different aerosol modes in the vertical because the ceilometer provides RCS profiles at only one wavelength. Hence, for the retrieval constraining intensive aerosol properties such as refractive indices, SSA, lidar ratio (LR) or effective radius are assumed equal for fine and coarse mode in the retrieval, which therefore implies that GRASP is not able to provide vertical profiles of these parameters. Column integrated retrieved parameter are aerosol size distribution (22 log-spaced triangle bins from 0.05 µm to 15 µm radius as in the operational AERONET retrievals) and fraction of spherical particles (also called sphere fraction). The scheme also provides column-integrated values of real refractive index (RRI), imaginary refractive index (IRI), SSA and LR at 5 wavelengths (440, 675, 870, 1020 and 1064 nm). However, the hypothesis of vertically constant aerosol intensive parameters allows changes in extensive properties and, therefore, vertical profiles of the 60 log-spaced bins of aerosol volume concentration and of extinction, backscatter, absorption and scattering coefficients at the mentioned 5 wavelengths are provided.

In the GRASP retrievals we assume: no changes in extensive vertical properties from ground to the z_{min} ; and an exponential decrease in these properties above z_{max} as in Lopatin et al. (2013). GRASP needs an initial aerosol scenario, also known as initial guess (Torres et al., 2017), to initialize each retrieval. The initial guess of each parameter has been assumed the same for all retrievals except for the size distribution, which has been assumed as a trapezoidal distribution proportional to the measured AOD at 440 nm wavelength (AOD_{440}). Finally, GRASP also provides the uncertainty, σ_G, on the retrieved parameters (VC, SSA, etc.), which is calculated from the random and systematic errors estimated by the detailed methodology shown in Sections 2.3 and 2.4 of Dubovik et al. (2000). These products obtained by GRASP using the described methodology are labelled in this work as $GRASP_{pac}$, which sub-index makes reference to the combination of "photometer and ceilometer". $GRASP_{pac}$ retrievals not showing convergence are rejected. Only 2% of the retrievals obtained in Section 5.2 were discarded by the convergence criteria.

4 Retrieval Sensitivity

4.1 Generation of Synthetic Data

A sensitivity study with synthetic data is done in order to observe the capability of the $GRASP_{pac}$. To this end, two kinds of aerosol are considered: Smoke and Dust, including different mixtures among them. Smoke and Dust typical size distributions and refractive indices are from Dubovik et al. (2002) for biomass burning in the African savanna (Zambia) and for desert dust at the Arabian Peninsula (Saudi Arabia), respectively. Figure 1 shows the typical size distributions for these two aerosol types (Fig. 1a) and their vertical distribution (Fig. 1b), real refractive index (Fig. 1c), and imaginary refractive index (Fig 1d) according to values reported in the bibliography.

The size distribution for each aerosol type (Figure 1a) are assumed as triangle binned and bimodal distribution: the fine mode is log-spaced in 10 radius bins (radius from 0.05 µm to 0.58 µm) and the coarse mode log-spaced in 15 bins (radius from 0.33 µm to 15 µm). Fine mode is predominant in Smoke aerosol with residual coarse mode, while for Dust the opposite occurs. We remember that for each scenario both fine and coarse mode have the same refractive indices, RRI being independent on wavelength with values of 1.51 and 1.56 for Smoke and Dust, respectively (Fig. 1c). The IRI is wavelength independent for Smoke, with a value of 0.021, while for Dust it is assumed variable with wavelength varying from 0.003 at 440 nm to 0.001 at 1064 nm (Fig. 1d). The vertical aerosol distribution has been assumed as an exponential decay with altitude for Smoke, while this distribution has been considered as a Gaussian layer centred at 2000 m a.g.l. for Dust (Fig. 1b).

Different synthetic scenarios are considered consisting to Smoke, Dust and mixtures among them. In the mixtures we assume that fine mode has the intensive properties of Smoke while for coarse mode they are those of Dust. Fine mode of size distribution is proportional to Smoke while that for coarse mode is proportional to Dust. Two different mixtures are considered, Mix-1 that imposes that AOD_{440} is equal for fine and coarse mode, and Mix-2 that imposes AOD at 1064 nm is equal for both modes. The difference between Mix-1 and Mix-2 is the larger volume concentration of fine particles in Mix-2 than in Mix-1. The size distribution and the vertical concentration for these scenarios can be observed in the figures discussed in Section 4.2, labeled as “Original” in Fig. 4 and 5, respectively. From all these scenarios, twelve (4 aerosol types x 3 AODs) synthetic data are computed from different AOD_{440} values: 0.1 (low aerosol load), 0.4 (minimum AOD_{440} used by AERONET to provide quality assured SSA, RRI and IRI in version 2 retrievals) and 1.0 (high aerosol load).

The GRASP forward model is used to compute the synthetic observations (spectral AOD, sky radiances and RCS at 1064 nm) following the conditions described in the flow diagram of Fig. 2 for each of the twelve aerosol scenarios, and varying the SZA by 10º from 40º to 80º in order to test different sets of scattering angles. Note that in all our simulations the ground is assumed as the sea level and the assumed BDRF parameters for these simulations are the climatological values (explained in Section 3.1.3) for Granada in summer. Later, using the GRASP forward model the required observations for $GRASP_{pac}$ are computed - AOD and sky radiances (26 values from 3.5º to 160º azimuth angles) at 440, 675, 870 and 1020 nm and RCS (60 heights) at 1064 nm.

The computed synthetic observations are not representative of real measurements unless instrument uncertainties are considered, which are ±0.01 for AOD and ±5% for sky radiances according to AERONET standards (Holben et al., 1998). Therefore, next step in the simulation scheme of Fig. 2 is to add uncertainties to the simulated AOD and sky radiances, which is done by adding random errors generated from random number that follows a normal distribution with standard deviation equal to the uncertainties. The addition of noise to the simulated values is done assuming a constant uncertainty (K) on raw ceilometer signal and, therefore, the uncertainty σ(RCS) varies with the square of the distance (z) and at a level 'z' is given as:

$$\sigma(RCS_z) = Kz^2 \tag{2}$$

where RCS_z is the range corrected signal at z.

The calibration constant for Granada ceilometer obtained by Cazorla et al. (2017) for molecular (aerosol free) regions presents variations with standard deviation of approximately 30% (result not published). Thus, the uncertainty of ceilometer RCS could be assumed as a 30% at the reference height (z_{ref}) where only molecular backscatter is detected. Then the uncertainty of RCS at z_{ref} can be written as:

$$\sigma\left(RCS_{z=z_{ref}}\right) = 0.3 * RCS_{z=z_{ref}} \tag{3}$$

and combining Eq. (2) and Eq. (3):

$$K = \frac{0.3}{{z_{ref}}^2} RCS_{z=z_{ref}} \tag{4}$$

Finally, if Eq. (4) is put in Eq. (2), the uncertainty of RCS at each height can be expressed as:

$$\sigma(RCS_z) = \frac{0.3}{{z_{ref}}^2} RCS_{z=z_{ref}} * z^2 \tag{5}$$

The most frequent value of z_{ref} obtained by the method used in Cazorla et al. (2017) is about 4000 m a.g.l.; therefore, in this work, the uncertainty of ceilometer RCS is calculated by Eq. (5) using 4000 m as z_{ref}.

Once RCS uncertainty has been characterized, synthetic RCS is interpolated every 15 m, and for each RCS value at 15 m at each scenario, a pseudorandom number normally distributed is generated with a standard deviation equal to the uncertainty of this RCS value, and this random number is added to the previously simulated RCS.

As an example, Fig. 3a shows the synthetic RCS after adding uncertainties for the Smoke and Mix-2 scenarios with AOD_{440} equal to 0.4. In addition, a particular example of measured RCS in Granada (dust case with AOD_{440} = 0.21) is included to illustrate the capabilities of our scheme to generate synthetic RCS with uncertainties. The iterative method to skip negative values in the measured RCS is applied to the initial values (Measured-Initial) and it is observed as the final signal avoids negative values (Measured-Final). As can be observed the profiles look noisier at higher heights both for the synthetic and measured profiles. In fact, the shape of the added noise to the synthetic profiles is very similar to the one observed in the real measurements, which indicates that the obtained synthetic signal can be considered as realistic. The noise is higher for Smoke likely because for this scenario molecular zone is not completely well represented by the assumed z_{ref} equal to 4000 m a.g.l. Figure 3b shows the RCS of Figure 3a normalized to the 60 heights required as input in GRASP. It can be appreciated that noise is reduced by the averaging of RCS in log-scaled bins.

4.2 Analyses of retrieved parameters

As the diagram of Fig. 2 shows, once the noisy synthetic observations are obtained for each aerosol scenario and SZA value, these data are used as input in

GRASP as explained in Section 3. The differences, Δ_{fit}, between the synthetic observations used as input in $GRASP_{pac}$ and the observations generated by the retrieved aerosol scenario are calculated to quantify the fitness of each $GRASP_{pac}$ retrieval (see Fig. 2). Δ_{fit} is defined as:

$$\Delta_{fit}(k,n) = O_r(k,n) - O_i(k,n) \tag{6}$$

and in percentage as:

$$\Delta_{fit}(k,n)(\%) = 100\% \frac{O_r(k,n) - O_i(k,n)}{O_i(k,n)} \tag{7}$$

where *O* represents an observation; the sub-index *i* and *r* indicated if the observation is an input or a value obtained from the retrieved aerosol scenario, respectively (see Fig. 2); *k* determines the kind of observation (AOD, sky radiances or RCS) and *n* is the number of this kind of observation. The fitness of the retrieval can be quantified for each *k*-kind observation by the mean (MBE; mean bias error) and standard deviation (STD) of Δ_{fit} using all *n* available observations for the *k*-kind. MBE represents the accuracy between O_r and O_i, while STD indicates their precision. Following this method, MBE and STD for AOD (sub-index *aod*), sky radiance (sub-index *rad*) and RCS (sub-index *rcs*) are calculated for all retrievals and they are shown in Table 1. MBE_{aod} and STD_{aod} are shown in absolute values while MBE and STD for sky radiance and RCS are in percentage. Scattering angle interval is also added in Table 1, reaching bigger angles when SZA increases. Table 1 reveals that MBE_{aod}, MBE_{rcs}, STD_{aod}, and STD_{rcs} are usually larger for retrievals with AOD_{440}=0.1; MBE_{rad} is usually within ±1% and STD_{rad} around 3%. In general, the fitness estimation does not show a clear dependence on aerosol type, SZA or AOD, which could indicate that differences in these values for different cases are mainly caused by the noise in the synthetic measurements since it is random.

Several aerosol $GRASP_{pac}$ products are obtained for each retrieval, but this work is mainly focus on columnar size distribution and especially on aerosol VC profiles. Figure 4 shows, for different aerosol types and loads, all the retrieved size distributions for various SZA values. We remind that errors were added to input optical data. The original size distributions are also included. In general, the retrieved size distributions look qualitatively similar to the original ones, especially for the coarse mode, for all aerosol scenarios. Discrepancies on fine mode are more evident especially at low AODs. Worse agreement is expected for small SZA values since the scattering angle range is shorter, however it is not observed. The differences between the original and retrieved size distributions are mostly related with Δ_{fit}. For example, the retrieved size distribution for Mix-1 type with AOD_{440}=0.4 differs more from the original at SZA equal to 60º than for the other angles; it should be caused by a worse fit between the inputs and the retrieved observations as it can be observed in Table 1, where MBE_{rad} and STD_{rad} reach their highest values (2.3% and 7.0%, respectively) for all retrievals with AOD_{440}=0.4. It can also be appreciated in the Mix-1 type with AOD_{440}=1.0 and SZA of 80º.

Figure 5 shows the VC profiles for the same data than in Fig. 4. These profiles show a good agreement with the original ones when coarse mode predominates as can be observed for Dust and Mix-1 cases. The larger differences between retrieved and reference profiles are found for Smoke, being particularly noisy for heights above 2 km. This worse agreement for Smoke could be due to the use of RCS at 1064 nm, this wavelength being less sensitive to the fine particles like those prevailing in Smoke. The original Mix-2 profiles present two intense aerosol layers: dust around 2 km and smoke below 1 km; $GRASP_{pac}$ method is able to detect both aerosol layers, although it shows discrepancies compared with the reference. This can be explained by the limited information of using RCS at only one wavelength. To quantify all the differences we defined Δ_{vc}, as the difference between the retrieved and original VC profiles (see Fig.2) given by:

$$\Delta_{vc}(a, SZA, z) = VC_r(k, SZA, z) - VC_o(a, SZA, z) \quad (8)$$

and in percentage as:

$$\Delta_{vc}(a, SZA, z)(\%) = 100\% \frac{VC_r(k,SZA,z) - VC_o(a,SZA,z)}{VC_o(a,SZA,z)} \quad (9)$$

where VC_r and VC_o represents the retrieved and original VC values, respectively (see Fig. 2); a determines the aerosol scenario (aerosol type and AOD_{440}) and z being one of the 60 bins of the retrieved VC profiles.

Table 2 shows the MBE and STD calculated as the mean and standard deviation, respectively, of the 60 Δ_{vc} values (Eq. (8) and (9)) of each profile. The Δ_{vc} values with VC_o below 1 $\mu m^3/cm^3$ have been discarded in the MBE and STD calculation since they could provide extreme differences in percentage. The results of Table 2 are showed for each of the 12 different aerosol scenarios and for different SZA. MBE and STD of Table 2 do not show any dependence with SZA. The best agreements (minima MBE and STD) are found for Dust and Mix-1 scenarios, where coarse mode is predominant. In general, unsigned MBE increases with AOD_{440} while the precision of $GRASP_{pac}$, given by STD, decreases in percentage with AOD_{440}. As a general result, for all scenarios together $GRASP_{pac}$ systematically underestimates VC showing a MBE of -5.9% and with an uncertainty, which is given by STD, of 21%. The lowest uncertainties of $GRASP_{pac}$ are for Dust aerosol (~14%) with bias close to zero, while the highest uncertainties are for the Smoke type (~28%).

In order to observe if the obtained differences between the original VC and the retrieved by $GRASP_{pac}$ are within σ_G (the estimation of retrieval uncertainty provided by

GRASP$_{pac}$), the percentage of unsigned Δ_{vc} values (Eq. (8)) that are below σ_G and $2\sigma_G$ have been calculated and named as $\Delta_{vc}<\sigma_G$ and $\Delta_{vc}<2\sigma_G$, respectively. If $\Delta_{vc}<\sigma_G$ and $\Delta_{vc}<2\sigma_G$ are similar to 68% and 95%, respectively, σ_G will represent the uncertainty in a good way indicating that Δ_{vc} is similar to a normal distribution with a standard deviation equal to σ_G. Table 3 shows the obtained results for each scenario shown in Table 2. $\Delta_{vc}<\sigma_G$ and $\Delta_{vc}<2\sigma_G$ do not show any dependence on SZA or AOD$_{440}$. Mix-2 aerosol scenario presents the $\Delta_{vc}<\sigma_G$ and $\Delta_{vc}<2\sigma_G$ values closer to 68% and 95%; Dust and Mix-1 show even higher values. Smoke aerosol shows the lowest values when all SZA and AOD$_{440}$ values are taken into account, but it is mainly caused by various individual cases with SZA=60º and AOD$_{440}$=0.1 or SZA=40º and AOD$_{440}$=1.0. For the combination of all the different aerosol scenarios, $\Delta_{vc}<\sigma_G$ is 74% and $\Delta_{vc}<2\sigma_G$ is 91%, which are close values to the expected 68% and 95%, and therefore we can conclude that GRASP$_{pac}$ reproduces well the VC profiles within the margins given by the uncertainty associated with the numerical inversion.

For backscatter and extinction coefficients at 1064 nm and column integrated intensive properties such as complex refractive index, SSA and LR we also did the same computations (not shown) as in Table 2 and Table 3. Combining all the data of the different aerosol scenarios MBE are -11% and -5% and STD equal to 31% and 21% for backscatter and extinction profiles, respectively. For the backscatter coefficient, MBE presents the largest values for Smoke and Mix-2, while Dust and Mix-2 show the largest STD values. In the case of the extinction coefficient, Dust and Mix-1 present the lowest STD (13% and 15%) and MBE (3% and 2%) values. Regarding the retrieved column-integrated SSA, considering the five wavelengths together, the retrieved SSA fits better the original values when AOD$_{440}$ increases, MBE being equal to -0.02, 0.01 and 0.00 and STD equal to 0.08, 0.05, and 0.02 for AOD$_{440}$ of 0.10, 0.4 and 1.0, respectively for all aerosol types and SZA values. The retrieved SSA also agrees better as SZA increases, indicating the importance of large scattering angles in this property as expected (Dubovik et al., 2000), but this dependence is only clear for AOD_{440}=0.4 and 1.0. Similar dependence on AOD_{440}, but not on SZA, appears for the retrieved LR. These LR retrievals agree with the references when all scenarios are considered together (MBE and STD are 10% and 29%). This agreement is found particularly for the Smoke aerosol cases. MBE and STD are reduced to 1% and 26% when only cases with AOD_{440}=0.4 are selected. Finally, for RRI and IRI, good agreements with the reference values are found for high AOD_{440}. Our last computations reveal that the differences between retrieved properties and the original ones are within σ_G, the obtained results indicate that σ_G of backscatter and extinction is representative of the real uncertainty for all AOD_{440} and SZA values. On the other hand, for SSA and LR the percentage of differences below σ_G is lower than the expected and showing an increase with AOD_{440}.

5 Results from inversion of real observations

5.1 Airborne comparison

Figure 6 shows the ceilometer RCS for the period 16-17th June 2013 where flights over Granada were done within the ChArMEx/ADRIMED field campaign. The largest RCS are observed below ~2 km a.s.l. that usually corresponds to aerosol in the planetary boundary layer (PBL). During this period, the study region was affected by Saharan dust outbreaks with transport of dust particles (Benavent-Oltra et al., 2017). The presence of long-range transported aerosol is clearly observed in Fig. 6 with significant signal up to 5 km a.s.l., approximately. Decoupled aerosol layers appeared from the 16th June evening to 17th morning, with aerosol entrainment in the PBL also observed, which is typically observed during Saharan dust arrivals at the study station

(Bravo-Aranda et al., 2015). Signal decreases are observed from 17th morning, particularly strong at low levels, and explained by advection of clean air-masses at these levels. However, a high-altitude layer remained at 3-5 km a.s.l.. The averaged (±standard deviation) daytime AOD at 440 nm and Angström Exponent (AE; in this work calculated only with the AOD at 440 and 870 nm) were 0.26±0.01 and 0.35±0.04 (63 data), respectively, for 16th June and 0.20±0.04 and 0.44±0.04 for 17th June (19 data); the low AE values indicate the presence of coarse particles. Five-day back-trajectories analyses using HYSPLIT model (Stein et al., 2015) (not shown) point out that the air masses came at Granada from the Saharan desert, which agrees with the presence of coarse particles as Saharan mineral dust.

Airplane spirals near the study region were done at 14:15-14:45 UTC (denoted as F30) and at 07:15-07:45 UTC (F31). F31 trajectory (similar to F30) is shown in Benavent-Oltra et al. (2017) and it shows that airborne measurements were done around 20 km far from Granada station. The time of both flights are marked in Figure 6 with black vertical lines while the closest GRASP$_{pac}$ retrieval to each flight is indicated by two green vertical lines, with AOD$_{440}$ of 0.27 and 0.21, respectively. The time difference of 2 hours between F30 flight and the closest GRASP$_{pac}$ retrieval is because limitations in SZA (at the exact time of the flight SZA was very small and become larger than 40º from 16:22 UTC). However, stable AOD measurements suggest not big aerosol variations during this 2 hour period.

Figure 7 shows the column-integrated size distribution, SSA, and refractive indices obtained by GRASP$_{pac}$ and these provided by AERONET (level 1.5). Comparisons of size distributions reveal that they are very similar between both methodologies, being the differences within the GRASP$_{pac}$ uncertainties. The size distributions also indicate the predominance of the coarse mode as expected for Saharan dust outbreaks (Valenzuela et al., 2012), and both retrievals point out a positive shift of the coarse mode concentration in the morning of 17th June. It is corroborated by the effective radius of the coarse mode given by $GRASP_{pac}$, which varied from 1.93 µm (Fig. 6a) to 2.22 µm (Fig. 6b). For SSA, Fig. 7c and 7d reveal that values are very similar between $GRASP_{pac}$ and AERONET, and both retrievals show a spectral dependence typical of mineral dust (Dubovik et al., 2002). RRI from AERONET is slightly higher in both cases than from $GRASP_{pac}$, but both retrievals show wavelength independence and a weak decrease from 16th to 17th June. Finally, for IRI again both AERONET and $GRASP_{pac}$ show similar patterns, typical for dust (Dubovik et al., 2002), and differences between methodologies are within the uncertainties. All these results point out that the column-integrated products from $GRASP_{pac}$ are in accordance with the ones provided by AERONET, at least in the analysed cases.

Figure 8 shows vertically-resolved values of particle VC from $GRASP_{pac}$ ($VC_{GRASP_{pac}}$) and the values obtained by airborne measurements ($VC_{Airborne}$). Generally both methodologies present very similar profiles for the two cases. For the flight F30, only one layer is observed with a slight and constant decrease up to 4.5 km approximately, while for F31 three different layers are observed. Most of the differences are within the $GRASP_{pac}$ uncertainty, however, disagreements are found between retrievals and airplane measurements for altitudes below 1.5 km, which can be explained because of the orography and air-traffic restriction that did not allow the flight to perform spiral exactly above the station. This reasoning agrees with the largest aerosol VC values at the lowest layer observed by GRASP retrievals, which can be associated with pollution from the city.

To quantify the differences between $GRASP_{pac}$ and airborne profiles, the VC from $GRASP_{pac}$ has been interpolated to the available heights of the airborne measurements. Point-by-point intercomparison between GRASP retrievals and airborne measurements are done. Linear interpolations of $GRASP_{pac}$ are done too for the same altitude than airborne measurements. Cases with very low aerosol load (VC<5 µm^3/cm^3) and measurements below 1.25 km a.s.l. (large disagreements in aerosol sampled between both techniques) are rejected in this comparison. Figure 9 shows particle VC obtained by GRASP versus airborne values. The correlation between both methodologies is high (correlation coefficient, *r*, higher than 0.80), and slightly better for F30 flight. However, the slope of the least square fit indicates that $GRASP_{pac}$ underestimates the highest airborne measurements and the abscissa intercept points out that $GRASP_{pac}$ overestimates the lowest values. In addition, the differences, ΔVC, between VC values from $GRASP_{pac}$ and airborne have been calculated as follows:

$$\Delta VC = VC_{GRASP_{pac}} - VC_{Airborne} \tag{10}$$

and in percentage as:

$$\Delta VC(\%) = 100\% \frac{VC_{GRASP_{pac}} - VC_{Airborne}}{VC_{Airborne}} \tag{11}$$

The histograms of ΔVC (Eq. (10)) are shown in Fig. 9d, 9e and 9f for F30, F31 and both flights, respectively. These graphs indicate that VC from $GRASP_{pac}$ agrees better with airborne measurements for F30 flight, being the 37% of the absolute ΔVC values below 2.5 µm^3/cm^3 and 89% below 7.5 µm^3/cm^3. The ΔVC distribution for F31 flight presents higher values but it is similar to a normal distribution, 61% of ΔVC absolute data being lower than 7.5 µm^3/cm^3; this percentage rises up to 75% when both flights are taken into account. Table 4 shows the mean (MBE), mean of the absolute values (MABE) and standard deviation (STD) of ΔVC (Eq. (10) and (11)) for these three cases of Fig. 9. $GRASP_{pac}$ slightly overestimates the $VC_{Airborne}$ values, showing MBE values of 10.5% and 12.9% for F30 and F31 flights, respectively; however, the absolute MBE is close to 0 μm^3/cm^3. Assuming airborne measurements as a reference, the accuracy, given by MBE, of VC from GRASP$_{pac}$ is below 12% when both flights are taken into account. Regarding MABE, F31 flight shows values around the double of that obtained from F30, which indicates that ΔVC differences are much higher in the F31 case, as STD confirms. The precision of GRASP$_{pac}$ using airborne measurements as a reference can be represented by STD, which presents a low value of 18.5% in the F30 case, but this value for F31 rises up to 70.8% due to the vertical shift of the lowest layer observed in Fig.8b. The STD for both flights together is 51.4%, but this value is still strongly affected by the differences in F31 flight for low heights. Finally, for both flights together, the percentage of ΔVC values which are below the uncertainty given by GRASP$_{pac}$ is 67.6%; this percentage is 94.4% when the double of the uncertainty is considered. These values are close to 68% and 95%, which points out that the uncertainty estimation provided by GRASP$_{pac}$ is representative of the real uncertainty of the retrieved VC.

5.2 High altitude station comparison

In-situ VC measurements during SLOPE I field campaign at the Sierra Nevada station (VC$_{SNS}$) are used for evaluating retrieved values by GRASP$_{pac}$ at the same altitude. In-situ measurements measured total particle VC in the range 0.05-10 μm and the GRASP$_{pac}$ retrieved values are integrated in the same range. From retrieved VC profiles, linear interpolations are done to have data at 2500 m a.s.l., which is the altitude of Sierra Nevada station. Figure 10 shows the temporal evolution of in-situ and retrieved VC values for the entire period. While measurements of VC$_{SNS}$ were continuous (24 hours per day), retrieved GRASP$_{pac}$ values are only available during some daytime points every day. The lack of VC$_{SNS}$ data during some short periods were caused by instrumental failures. From Figure 10 can be observed that both measured and retrieved values follow the same temporal evolution, with minimum values associated with clean atmosphere and extreme values associated mostly to Saharan dust arrivals. In fact, the largest values at Sierra Nevada were registered during the morning of 21st July, with in-situ measurements up to 269 $\mu m^3/cm^3$ and retrieved $GRASP_{pac}$ values from 279 to 364 $\mu m^3/cm^3$, and were associated with a strong Saharan dust episode that started on 20th July 2016.

Figure 11a shows a normalized number density plot of retrieved values by $GRASP_{pac}$ versus in-situ measurements (VC_{SNS}). Selected in-situ measurements are averaged during a time period of ±15 min from the retrieval time. Most of the VC values on Figure 11a are below 20 $\mu m^3/cm^3$, being 71% for VC_{SNS}. The linear fit reveals an overestimation of VC from $GRASP_{pac}$ to the VC_{SNS} values around 50%. The data for 26th August can be partially responsible of this overestimation with $VC_{GRASP_{pac}}$ values ~150 $\mu m^3/cm^3$ while VC_{SNS} is ~50 $\mu m^3/cm^3$. These larger differences could be in part due to real differences in the aerosol over the Granada vertical and the aerosol at Sierra Nevada, since SNS could be affected by local effects and sources.

The correlation between $VC_{GRASP_{pac}}$ and VC_{SNS} is high, being r equal to 0.91; this correlation coefficient is higher than the obtained between the ground measured AOD_{440} and VC_{SNS}, which is 0.79, and the correlation between the retrieved column-integrated VC and VC_{SNS}, which is 0.80. This result points out that the addition of ceilometer signal to the aerosol retrieval improves the capacity to estimate the aerosol vertical concentration.

As in Section 5.1, the differences ΔVC between $VC_{GRASP_{pac}}$ and the in-situ measurements, in this case VC_{SNS}, have been calculated. ΔVC can be expressed as:

$$\Delta VC = VC_{GRASP_{pac}} - VC_{SNS} \tag{12}$$

and in percentage as:

$$\Delta VC(\%) = 100\% \frac{VC_{GRASP_{pac}} - VC_{SNS}}{VC_{SNS}} \tag{13}$$

Figure 11b shows the ΔVC (Eq. (12)) distribution. This frequency histogram is similar to a normal distribution, the maximum being centred close to 0; however it is skewed to positive values. 38%, 73% and 87% of $VC_{GRASP_{pac}}$ shows absolute ΔVC differences lower than 2.5, 7.5 and 12.5 µm^3/cm^3, respectively.

Table 5 shows mean values and standard deviations of the differences ΔVC, from Eq. (12) and (13), for different VC_{SNS} ranges. The percentages of data when ΔVC is lower than the numerical uncertainty in the inversion, σ_G, are also included. From Table 5 when all ranges of VC are considered mean differences and standard deviations are 31% and 94%, both strongly affected by the low values of VC_{SNS}. In fact, MBE and STD are 64% and 169%, respectively, for VC_{SNS} values only below 5 µm^3/cm^3. However, if only data with VC_{SNS} above 5 µm^3/cm^3 are selected (493 in total), mean difference and standard deviations are reduced to 23% and 59%, respectively. In general, MBE increases with VC_{SNS} ranging from 10% to 60% if VC_{SNS} below 5 µm^3/cm^3 is not considered. MABE presents values around 40-50% for VC_{SNS} between 5 and 100 µm^3/cm^3. STD varies from 34-64%, showing the lowest values for highest concentrations. Regarding the ΔVC differences within the $GRASP_{pac}$ uncertainty estimation, Table 5 shows values below that expected, which indicates that the VC uncertainty estimation provided by $GRASP_{pac}$ could be not representative of the real uncertainty in this case. However, the obtained results could be affected by different factors, independent of $GRASP_{pac}$, which yield a worse agreement than in the airborne comparison of Section 5.1. In this section the aerosol properties in the free vertical atmosphere over Granada have been assumed equal to the properties at the surface on Sierra Nevada ground station, which could be affected by other aerosol sources and atmospheric conditions. Moreover, the instrumental uncertainty on VC_{SNS} could be also partially responsible of the observed differences.

Figure 12 shows the differences ΔVC of Eq. (12) as function of VC_{SNS} (Fig. 12a), AOD_{440} (Fig. 12b), Angström Exponent (Fig. 12c) and sphere fraction (Fig. 12d). Generally it is observed that ΔVC increases with VC_{SNS}, however, some high ΔVC values appear for moderate VC_{SNS} values which correspond to the mentioned case of 26th August. ΔVC also increases with AOD_{440}, however high ΔVC values do not appear for moderate AOD_{440} and even low ΔVC values can be observed for high AOD_{440}. ΔVC does not show any clear dependence on AE and sphere fraction, except the highest ΔVC values for the lowest values of AE and sphere fraction, which mainly corresponds to dust particles during the mentioned strong dust episode of 20th -21st July 2016 (see Fig. 10).

Finally, a case of study based on the dust episode of 20th -21st July 2016 has been analysed as an illustration. Figure 13a and 13b show the retrieved VC profiles and the measured VC_{SNS} at Sierra Nevada on the afternoon of 20th July and on the morning of 21st July, respectively. The AOD_{440} from Granada was 0.85 and 0.83 for the Fig. 13a and 13b, respectively, which indicates very similar aerosol load. It indicates that in columnar terms, both cases are similar, but if ceilometer measurements are added to the retrieval, the vertical distribution can be discerned; this is the case in Fig. 13, where the $GRASP_{pac}$ retrieval indicates that VC at SNS increased by about four times from 20th to 21st July, which was also appreciated in the measurements of VC_{SNS}. Then, thanks to ceilometer addition, it is known that the dust episode came 20th July in a strong layer located between 3.5-4.0 km a.s.l.. This layer went down providing extreme values at

SNS height in the morning of 21st July, but also high dust concentrations in lower heights, which did not happen in the evening of 20th July.

6 Conclusions

In this work we have explored the use of collocated sun/sky photometer and ceilometer measurements in the General Retrieval of Aerosol and Surface Properties (GRASP) code to retrieve column-integrated and vertically-resolved optical and microphysical aerosol properties such as backscatter and extinction coefficients and volume concentration, among others. The capability to combining such set of measurements and using them in GRASP has been studied through different sets of simulations for typical dust and biomass-burning aerosol located at different altitudes as well as mixtures of both. In general, the proposed GRASP retrievals reproduce better aerosol properties for coarse particles, likely due to the operational long wavelength of the ceilometer at 1064 nm, and for high aerosol optical depth values. The results of the simulations have demonstrated good agreements for column-integrated size distributions and optical parameters such as complex refractive indices and single scattering albedo. For vertically-resolved aerosol properties, volume concentration presents an accuracy of -6% and an uncertainty of 21%; this accuracy is -11% and 5% for backscatter and extinction profiles at 1064 nm, being the uncertainty 31% and 21%, respectively. The mentioned analysis concludes that the uncertainty of these GRASP retrievals is representative of the real uncertainty of the retrieved parameters, except for column single scattering albedo and lidar ratio where the uncertainty given by GRASP is only representative when aerosol optical depth increases.

Two case studies from mid-June 2013 documented during the ChArMEx/ADRIMED field campaign have allowed the comparison of retrieved vertical profiles versus airborne in-situ measurements. The aerosol volume concentration obtained by GRASP presents high correlation with the measured one during the two flights. Differences in this concentration between GRASP retrievals and airborne measurements present a mean value below 12% and a standard deviation around 51%. All these differences are within the uncertainty estimations provided by the GRASP code. Moreover, comparisons of the column-integrated retrieved parameters by the proposed scheme for GRASP versus AERONET retrievals have been done showing a good agreement between both techniques (differences were within uncertainties).

Data acquired during the SLOPE I field campaign (summer 2016) at the high mountain Sierra Nevada station, located at 2500 m a.s.l, were used to evaluate the retrieved aerosol volume concentration at a certain altitude. The in-situ volume concentration at a mountain station in Sierra Nevada correlates better (r=0.91) with the aerosol volume concentration obtained by GRASP at 2500 m a.s.l. than other variables like aerosol optical depth at Granada (ground station). Discarding the lowest concentration values, the mean differences between retrieved and the measured volume concentrations are of 23% with a standard deviation of 59%, which means that GRASP frequently overestimates the in-situ measurements at Sierra Nevada. However, part of these differences could be caused by uncertainties in the in-situ measurements and assumptions, and in the fact that the aerosol over Granada (where ceilometer monitoring was performed) could not be the same than the aerosol on Sierra Nevada, which could be affected by local dynamic and atmospheric effects, and also to local aerosol sources at the high mountains.

Overall, the obtained results indicate that the combination of sun/sky photometer and ceilometer measurements and their use as inputs in GRASP provides reliable products if the uncertainties are considered. Nevertheless, the experimental data obtained were mostly representative of dust and clean conditions, and more evaluations are required for very polluted environment and intense biomass-burning. Therefore, as outlook, the method could be applied in different places, using networks like ICENET, and in long time series in order to characterize the regional and temporal changes on vertical aerosol extensive properties.

Acknowledgements

This work was supported by the Andalusia Regional Government (project P12-RNM-2409) and by the “Consejería de Educación" of "Junta de Castilla y León" (project VA100U14); the Spanish Ministry of Economy and Competitiveness under the projects, CMT2015-66742-R, CGL2016-81092-R and “Juan de la Cierva-Formación” program (FJCI-2014-22052); and the European Union’s Horizon 2020 research and innovation programme through project ACTRIS-2 (grant agreement No 654109) and the Marie Curie Rise action GRASP-ACE (grant agreement No 778349). The authors thankfully acknowledge the FEDER program for the instrumentation used in this work. COST Action TOPROF (ES1303), supported by COST (European Cooperation in Science and Technology), is also acknowledged. The authors acknowledge the use of GRASP inversion algorithm (www.grasp-open.com). The MODIS MCD43C1 data product was retrieved from the online Data Pool, courtesy of the NASA Land Processes Distributed Active Archive Center (LP DAAC), USGS/Earth Resources Observation and Science (EROS) Center, Sioux Falls, South Dakota, https://lpdaac.usgs.gov/data_access/data_pool. This work contributes to WP4 on aerosol-radiation-climate interaction of the ChArMEx project supported by ADEME, CEA, CNRS-INSU and Météo-France through the multidisciplinary programme

MISTRALS (Mediterranean Integrated Studies aT Regional And Local Scales). We thank the instrument scientists, pilots and ground crew of SAFIRE for facilitating the instrument integration and conducting flight operations.

References

Ansmann, A., Riebesell, M., Weitkamp, C. (1990): Measurement of atmospheric aerosol extinction profiles with a Raman lidar. Opt. Lett. 15, 746–748.

Ansmann, A., Baars, H., Tesche, M., Müller, D., Althausen, D., Engelmann, R., Pauliquevis, T., Artaxo, P. (2009): Dust and smoke transport from Africa to South America: Lidar profiling over Cape Verde and the Amazon rainforest. Geophys. Res. Lett., 36, 11, L11802, doi:10.1029/2009GL037923.

Ansmann, A., Seifert, P., Tesche, M., Wandinger, U. (2012): Profiling of fine and coarse particle mass: case studies of Saharan dust and Eyjafjallajökull/Grimsvötn volcanic plumes. Atmos. Chem. Phys, 12, 20, 9399-9415.

Barreto, A., Cuevas, E., Damiri, B., Berkoff, T., Berjón, A.J., Hernández, Y., Almansa, F., Gil, M. (2013): A new Method for nocturnal aerosol measurements with a lunar photometer prototype. Atmos. Meas. Tech., 6, 585–598.

Barreto, A., Cuevas, E., Granados-Muñoz, M.J., Alados-Arboledas, L., Romero, P.M., Gröbner, J., Kouremeti, N., Almansa, A.F., Stone, T., Toledano, C., Román, R., Sorokin, M., Holben, B., Canini, M., Yela, M. (2016): The new sun-sky-lunar Cimel CE318-T multiband photometer – a comprehensive performance evaluation. Atmos. Meas. Tech., 9, 631–654, doi.org/10.5194/amt-9-631-2016.

Baumgardner, D., Dye, J.E., Gandrud, B.W., Knollenberg, R.G. (1992): Interpretation of measurements made by forward scattering probe (FSSP-300) during the airborne arctic stratospheric expedition, J. Geophys. Res., 97, 8035–8046, doi:10.1029/91JD02728.

Benavent-Oltra, J.A., Román, R., Granados-Muñoz, M.J., Pérez-Ramírez, D., Ortiz-Amezcua, P., Denjean, C., Lopatin A., Lyamani, H., Torres, B., Guerrero-Rascado, J. L., Fuertes, D., Dubovik, O., Chaikovsky, A., Olmo, F.J., Mallet, M., Alados-Arboledas, L. (2017): Comparative assessment of GRASP algorithm for a dust event over Granada (Spain) during ChArMEx-ADRIMED 2013 campaign. Atmos. Meas. Tech., 10, 4439-4457, doi:10.5194/amt-2017-200.

Böckmann, C. (2001): Hybrid regularization method for the ill-posed inversion of multiwavelenght lidar data to determine aerosol size distributions, Appl. Opt., 40, 1329-1342.

Boucher, O., Randall, D., Artaxo, P., Bretherton, C., Feingold, G., Forster, P., Kerminen, V.-M., Kondo, Y., Liao, H., Lohmann, U., Rasch, P., Satheesh, S.K., Sherwood, S., Stevens, B., Zhang, X.Y. (2013): Clouds and aerosols. In Climate change 2013: the physical science basis. Contribution of Working Group I to the Fifth Assessment Report of the Intergovernmental Panel on Climate Change, 571-657. Cambridge University Press, United Kingdom and New York, NY, USA.

Bovchaliuk, V., Goloub, P., Podvin, T., Veselovskii, I., Tanre, D., Chaikovsky, A., Dubovik, O., Mortier, A., Lopatin, A., Korenskiy, M., Victori, S. (2016): Comparison of aerosol properties retrieved using GARRLiC, LIRIC, and Raman algorithms applied to multi-wavelength LIDAR and sun/sky-photometer data. Atmos. Meas. Tech., 9, 3391-3405, doi.org/10.5194/amt-9-3391- 2016.

Bravo-Aranda, J.A., Navas-Guzmán, F., Guerrero-Rascado, J.L., Pérez-Ramírez, D., Granados-Muñoz, M.J., Alados-Arboledas L. (2013): Analysis of lidar depolarization calibration procedure and application to the atmospheric aerosol characterization, Int. J. Remote Sens., 34, 9–10, 3543–3560.

Bravo-Aranda, J.A., Titos, G., Granados-Muñoz, M.J., Guerrero-Rascado, J.L., Navas-Guzmán, F., Valenzuela, A., Lyamani, H., Olmo, F.J., Andrey, J., and Alados-Arboledas L. (2015): Study of mineral dust entrainment in the planetary boundary layer by lidar depolarisation technique. Tellus B, 67, 1, 26180, doi.org/10.5194/amt-9-3391-2016.

Burton, S.P., Ferrare, R.A., Hostetler, C.A., Hair, J.W., Rogeres, R.R., Obland, M.D., Obland, M.D., Butler, C.F., Cook, A.L., Harper, D.B., Froyd., K.D. (2012): Aerosol classification using airborne High Spectral Resolution Lidar measurements - methodology and examples. Atmos. Meas. Tech., 5, 73-98.

Cai, Y., Montague, D.C., Mooiweer-Bryan, W., Deshler, T. (2008): Performance characteristics of the ultra high sensitivity aerosol spectrometer for particles between 55 and 800 nm: Laboratory and field studies. J. Aerosol Sci., 39, 759–769, doi:10.1016/j.jaerosci.2008.04.007.

Cazorla, A., Casquero-Vera, J.A., Román, R., Guerrero-Rascado, J.L., Toledano, C., Cachorro, V.E., Orza, J.A.G., Cancillo, M.L., Titos, G., Pandolfi, M., Alastuey, A., Hanrieder, N., Alados-Arboledas, L. (2017): Near real time processing of ceilometer network data: Characterizing an extraordinarty dust outbreak over the Iberian Peninsula. Atmos. Chem. Phys., 17, 11861-11876, doi:10.5194/acp-17-11861-2017.

Chaikovsky, A., Dubovik, O., Goloub, P., Balashevich, N., Lopatsin, A., Karol, Y., Denisov, S., Lapyonok, T. (2008): Software package for the retrieval of aerosol microphysical properties in the vertical column using combined lidar/photometer data (test version), Technical Report, Minsk, Belarus, Institute of Physics, National Academy of Sciences of Belarus.

Chaikovsky, A., Dubovik, O., Holben, B., Bril, A., Goloub, P., Tanré, D., Pappalardo, G., Wandinger, U., Chaikovskaya, L., Denisov, S., Grudo, J., Lopatin, A., Karol, Y., Lapyonok, T., Amiridis, V., Ansmann, A., Apituley, A., Allados-Arboledas, L., Binietoglou, I., Boselli, A., D'Amico, G., Freudenthaler, V., Giles, D., Granados-Muñoz, M. J., Kokkalis, P., Nicolae, D., Oshchepkov, S., Papayannis, A., Perrone, M. R., Pietruczuk, A., Rocadenbosch, F., Sicard, M., Slutsker, I., Talianu, C., De Tomasi, F., Tsekeri, A., Wagner, J., Wang, X. (2016): Lidar-Radiometer Inversion Code (LIRIC) for the retrieval of vertical aerosol properties from combined lidar/radiometer data: development and distribution in EARLINET, Atmos. Meas. Tech., 9, 1181-1205, doi:10.5194/amt-9-1181-2016.

Chemyakin, E., Burton, S., Kolgotin, A., Müller, D., Hostetler, C., Ferrare, R. (2016) Retrieval of aerosol parameters from multiwavelength lidar: investigation of the underlying inverse mathematical problem. Appl. Opt., 55, 2188-2202.

De Haij, M., Wauben, W., Baltink, H. K. (2007). Continuous mixing layer height determination using the LD-40 ceilometer: a feasibility study. KNMI report WR-2007-01, KNMI, De Bilt, The Netherlands.

Denjean, C., Cassola, F., Mazzino, A., Triquet, S., Chevaillier, S., Grand, N., Bourrianne, T., Momboisse, G., Sellegri, K., Schwarzenbock, A., Freney, E., Mallet, M., Formenti, P. (2016): Size distribution and optical properties of mineral dust aerosols transported in the western Mediterranean, Atmos. Chem. Phys., 16, 1081-1104, doi:10.5194/acp-16-1081-2016.

Dubovik, O., King, M. D. (2000): A flexible inversion algorithm for retrieval of aerosol optical properties from Sun and sky radiance measurements. J. Geophys. Res. Atmos., 105, 20673–20696.

Dubovik, O., Smirnov, A., Holben, B.N., King, M.D., Kaufman, Y.J., Eck, T.F., Slutsker, I. (2000): Accuracy assessments of aerosol optical properties retrieved from Aerosol Robotic Network (AERONET) Sun and sky radiance measurements. J. Geophys. Res., 105, D8, 9791–9806, doi:10.1029/2000JD900040.

Dubovik, O., Holben, B., Eck, T.F., Smirnov, A., Kaufman, Y.J., King, M.D., Tanre, D., Slutsker, I. (2002): Variability of absorption and optical properties of key aerosol types observed in worldwide locations J. Atmos. Sci., 59, 590–608.

Dubovik, O., Sinyuk, A., Lapyonok, T., Holben, B.N., Mishchenko, M., Yang, P., Eck, T., Volten, H., Munoz, O., Veihelmann, B., Van Der Zande, W.J., Leon, J., Sorokin, M., Slutsker, I. (2006): Application of spheroid models to account for aerosol particle nonsphericity in remote sensing of desert dust. J. Geophys. Res. Atmos., 111, D11208, doi.org/10.1029/2005JD006619.

Dubovik, O., Lapyonok, T., Litvinov, P., Herman, M., Fuertes, D., Ducos, F., Lopatin, A., Chaikovsky, A., Torres, B., Derimian, Y., Huang, X., Aspetsberger, M., Federspiel, C. (2014): GRASP: a versatile algorithm for characterizing the atmosphere. SPIE: Newsroom 10.1117/2.1201408.005558.

Emeis, S. and Forkel, R. Junkermann, W. Schafer, K. Flentje, H. Gilge, S. Fricke, W. Wiegner, M. Freudenthaler, V. Gross, S. Ries, L. Meinhardt, F. Birmili, W. Munkel, C. Obleitner, F., Suppan, P. (2011). Measurement and simulation of the 16/17 April 2010 Eyjafjallajökull volcanic ash layer dispersion in the northern Alpine region. Atmos. Chem. Phys., 11, 2689-2701.

Espinosa, W.R., Remer, L.A., Dubovik, O., Ziemba, L., Beyersdorf, A., Orozco, D., Schuster, G., Lapyonok, T., Fuertes, D., Martins, J.V. (2017). Retrievals of aerosol optical and microphysical properties from Imaging Polar Nephelometer scattering measurements. Atmos. Meas. Tech., 10, 811-824.

Fedarenka, A., Dubovik, O., Goloub, P., Li, Z., Lapyonok, T., Litvinov, P., Blarel, L., Gonzalez, L., Podvin, T., Crozel, D. (2016): Utilization of AERONET polarimetric measurements for improving retrieval of aerosol microphysics: GSFC, Beijing and Dakar data analysis. J. Quant. Spectrosc. Radiat. Transfer, 179, 72-97.

Fernald F.G. (1984): Analysis of atmospheric lidar observations: some comments. Appl. Opt., 23, 652–653.

Flentje, H., Claude, H., Elste, T., Gilge, S., Köhler, U., Plass-Dülmer, C., Steinbrecht, W., Thomas, W., Werner, A., Fricke, W. (2010). The Eyjafjallajökull eruption in April 2010–detection of volcanic plume using in-situ measurements, ozone sondes and lidar-ceilometer profiles. Atmos. Chem. and Phys., 10, 10085-10092. doi:10.5194/acp-10-10085-2010.

Granados-Muñoz, M.J., Bravo-Aranda, J.A., Baumgardner, D., Guerrero-Rascado, J.L., Pérez-Ramírez, D., Navas-Guzmán, F., Veselovskii, I., Lyamani, H., Valenzuela, A., Olmo, F.J., Titos, G., Andrey, J., Chaikovsky, A., Dubovik, O., Gil-Ojeda, M., Alados-Arboledas, L. (2016): A comparative study of aerosol microphysical properties retrieved from ground-based remote sensing and aircraft in situ measurements during a Saharan dust event. Atmos. Meas. Tech., 9, 1113-1133, doi.org/10.5194/amt9-1113-2016.

Gross, S., Esselborn, M., Weinzierl, B., Wirth, M., Fix, A., Petzold, A. (2013): Aerosol classification by airborne high spectral resolution lidar observations. Atmos. Chem. Phys., 13, 5, 2487-2505.

Haeffelin, M., Laffineur, Q., Bravo-Aranda, J.-A., Drouin, M.-A., Casquero-Vera, J.-A., Dupont, J.-C., De Backer, H. (2016). Radiation fog formation alerts using attenuated backscatter power from automatic lidars and ceilometers, Atmos. Meas. Tech., 9, 5347-5365. doi.org/10.5194/amt-9-5347-2016.

Heese, B., Flentje, H., Althausen, D., Ansmann, A., Frey, S. (2010). Ceilometer lidar comparison: backscatter coefficient retrieval and signal-to-noise ratio determination. Atmos. Meas. Tech., 3, 6, 1763-1770.

Holben, B.N., Eck, T.F., Slutsker, I., Tanré, D., Buis, J.P., Setzer, A., Vermote, E., Reagan, J. A., Kaufman, Y. J., Nakajima, T., Lavenu, F., Jankowiak, I., Smirnov A. (1998): AERONET – A federated instrument network and data archive for aerosol characterization. Remote Sens. Environ., 66, 1–16.

Holben, B. N., Eck, T. F., Slutsker, I., Smirnov, A., Sinyuk, A., Schafer, J., Giles, D., Dubovik, O. (2006): AERONET's version 2.0 quality assurance criteria. Proc. SPIE 6408, Remote Sensing of the Atmosphere and Clouds, 64080Q (November 28, 2006); doi:10.1117/12.706524.

Jenoptik (2013): CHM15k – Nimbus Ceilometer User Manual. Revision P0, September 2013.

Klett J.D. (1981): Stable analytical inversion solution for processing lidar returns. Appl. Opt., 20, 211–220.

Klett J.D. (1985): Lidar inversion with variable backscatter/extinction ratios. Appl. Opt., 24, 1638–1643.

Kokhanovsky, A.A., Davis, A.B., Cairns, B., Dubovik, O., Hasekamp, O.P., Sano, I., Mukai, S., Rozanov, V.V., Litvinov, P., Lapyonok, T., Kolomiets, I.S., Oberemok, Y.A., Savenkov, S., Martin, W., Wasilewski, A., Di Noia, A., Stap, F.A., Rietjens, J., Xu, F., Natraj, V., Duan, M., Cheng, T., Munro, R. (2015): Space-based remote sensing of atmospheric aerosols: The multi-angle spectro-polarimetric frontier. Earth-Science Reviews, 145, 85-116.

Li, X., Strahler, A.H. (1992): Geometric-optical bidirectional reflectance modeling of the discrete crown vegetation canopy: Effect of crown shape and mutual shadowing. IEEE transactions on Geoscience and Remote Sensing, 30, 2, 276-292.

Li, S., Everette, J., Min, Q., Yin, B., Sakai, R., Payne, M.K. (2017): Remote sensing of PM2. 5 during cloudy and nighttime periods using ceilometer backscatter. Atmos. Meas. Tech., 10, 2093–2104.

Lopatin, A., Dubovik, O., Chaikovsky, A., Goloub, P., Lapyonok, T., Tanré, D., Litvinov, P. (2013): Enhancement of aerosol characterization using synergy of lidar and sun-photometer coincident observations: the GARRLiC algorithm. Atmos. Meas. Tech., 6, 2065–2088, doi:10.5194/amt-6-2065-2013.

Lyamani, H., Olmo F.J., Alados-Arboledas, L. (2010): Physical and optical properties of aerosols over an urban location in Spain: seasonal and diurnal variability. Atmos. Chem. Phys., 10, 239–254.

Lyamani, H., Olmo, F.J., Foyo, I., Alados-Arboledas, L. (2011): Black carbon aerosols over an urban area in south-eastern Spain: changes detected after the 2008 economic crisis. Atmos. Environ. 45, 6423-6432.

Madonna, F., Amato, F., Vande Hey, J., Pappalardo, G. (2015): Ceilometer aerosol profiling versus Raman lidar in the frame of the INTERACT campaign of ACTRIS. Atmos. Meas. Tech., 2207-2223.

Mallet, M., Dulac, F., Formenti, P., Nabat, P., Sciare, J., Roberts, G., Pelon, J., Ancellet, G., Tanré, D., Parol, F., Denjean, C., Brogniez, G., di Sarra, A., Alados-Arboledas, L., Arndt, J., Auriol, F., Blarel, L., Bourrianne, T., Chazette, P., Chevaillier, S., Claeys, M., D'Anna, B., Derimian, Y., Desboeufs, K., Di Iorio, T., Doussin, J.-F., Durand, P., Féron, A., Freney, E., Gaimoz, C., Goloub, P., Gómez-Amo, J. L., Granados-Muñoz, M. J., Grand, N., Hamonou, E., Jankowiak, I., Jeannot, M., Léon, J.-F., Maillé, M., Mailler, S., Meloni, D., Menut, L., Momboisse, G., Nicolas, J., Podvin, T., Pont, V., Rea, G., Renard, J.-B., Roblou, L., Schepanski, K., Schwarzenboeck, A., Sellegri, K., Sicard, M., Solmon, F., Somot, S., Torres, B., Totems, J., Triquet, S., Verdier, N., Verwaerde, C., Waquet, F., Wenger, J., Zapf, P. (2016): Overview of the Chemistry-Aerosol Mediterranean Experiment/Aerosol Direct Radiative Forcing on the Mediterranean Climate (ChArMEx/ADRIMED) summer 2013 campaign. Atmos. Chem. Phys., 16, 455-504, doi:10.5194/acp-16-455-2016.

Mandija, F., Sicard, M., Comerón, A., Alados-Arboledas, L., Guerrero-Rascado J.L., Barragan, R., Bravo-Aranda, J.A., Granados-Muñoz, M-J, Lyamani, H., Muñoz Porcar, C., Rocadenbosch, F., Rodríguez, A., Valenzuela, A., García Vizcaíno, D. (2016): Origin and pathways of the mineral dust transport to two Spanish EARLINET sites: Effect on the observed columnar and range-resolved dust optical properties, Atmospheric Research, 187, 69-83, doi: 10.1016/j.atmosres.2016.12.002.

Martucci, G., Milroy, C., O'Dowd, C.D. (2010): Detection of cloud-base height using Jenoptik CHM15K and Vaisala CL31 ceilometers. J. Atmos. Ocean. Tech., 27, 2, 305-318.

Müller, D., Wandinger, U., and Ansmann, A. (1999): Microphysical particle parameters from extinction and backscatter lidar data by inversion with regularization: simulation. Appl. Opt., 38, 2358-2368.

Müller, D., Mattis, I., Ansmann, A., Wehner, B., Althausen, D., Wandinger, U., Dubovik, O. (2004): Closure study on optical and microphysical properties of a mixed urban and Arctic haze air mass observed with Raman lidar and Sun photometer. J. Geophys. Res., 109, D13206.

Münkel, C., Eresmaa, N., Räsänen, J., Karppinen, A. (2007): Retrieval of mixing height and dust concentration with lidar ceilometer. Boundary-layer meteorology, 124, 1, 117-128.

Navas-Guzmán, F., Müller, D., Bravo-Aranda, J.A., Guerrero-Rascado, J.L., Granados-Muñoz, M.J., Pérez-Ramírez, D., Olmo, F.J., Alados-Arboledas, L. (2013): Eruption of the Eyjafjallajökull Volcano in spring 2010: Multiwavelength Raman lidar measurements of sulphate particles in the lower troposphere. J. Geophys. Res., 118, 1804-1813.

Noh, Y.M., Müller, D., Shin, D.H., Lee, H., Jung, J.S., Lee, K.H., Cribb, M., Li, Z., Kim, Y.J. (2009): Optical and microphysical properties of severe haze and smoke aerosol measured by integrated remote sensing techniques in Gwangju, Korea. Atmos. Environ., 43, 879-888.

Ortiz-Amezcua, P., Guerrero-Rascado, J. L., Granados-Muñoz, M. J., Benavent-Oltra, J. A., Böckmann, C., Samaras, S., Stachlewska, I. S., Janicka, Ł., Baars, H., Bohlmann, S., Alados-Arboledas, L. (2017): Microphysical characterization of long-range transported biomass burning particles from North America at three EARLINET stations. Atmos. Chem. Phys., 17, 5931-5946, https://doi.org/10.5194/acp-17-5931-2017.

Pappalardo, G., Amodeo, A., Apituley, A., Comeron, A., Freudenthaler, V., Linne, H., Ansmann, A., Bosenberg, J., D'Amico, G., Mattis, I., Mona, L., Wandinger, U., Amiridis, V., Alados-Arboledas, L., Nicolae, D., Wiegner, M. (2014): EARLINET: towards an advanced sustainable European aerosol lidar network, Atmos. Meas. Tech., 7, 2389-2409, doi.org/10.5194/amt7-2389-2014.

Pérez-Ramírez, D., Lyamani, H., Olmo, F.J., Whiteman, D.N., and Alados-Arboledas, L. (2012): Columnar aerosol properties from sun-and-star photometry: statistical comparisons and day-to-night dynamic. Atmos. Chem. Phys., 12, 9719-9738.

Pérez-Ramírez, D., Lyamani, H., Smirnov, A., O'Neill, N.T., Veselovskii, I., Whiteman, D.N., Olmo, F.J., Alados-Arboledas, L. (2016): Statistical study of day and night hourly patterns of columnar aerosol properties using sun and star photometry. Proc. of SPI Vol. 10001, 100010K. in Remote Sensing of Clouds and the Atmosphere XXI. Edited by Adolfo Comeron, Evgueni I. Kassianov, Klaus Schafer, James W. Jack, Richard H. Picard and Konradin Weber.

Prata, A.J. (2009): Satellite detection of hazardous volcanic clouds and the risk to global air traffic. Nat. hazards, 5, 303-324.

Román, R., Torres, B., Fuertes, D., Cachorro, V.E., Dubovik, O., Toledano, C., Cazorla, A., Barreto, A., Bosch, J.L., Lapyonok, T., González, R., Goloub, P., Perrone, M.R., Olmo, F.J., de Frutos, A., Alados-Arboledas, L. (2017a): Remote sensing of lunar aureole with a sky camera: Adding information in the nocturnal retrieval of aerosol properties with GRASP code. Remote Sens. Environ., 196, 238-252, doi.org/10.1016/j.rse.2017.05.013.

Román, R., Cazorla, A., Toledano, C., Olmo, F. J., Cachorro, V. E., de Frutos, A., Alados-Arboledas, L. (2017b): Cloud cover detection combining high dynamic range sky images and ceilometer measurements. Atmos., Res., 196, 224–236.

Ross, J. (1981): The radiation regime and architecture of plant stands. The Hague, The Netherlands: Dr. W. Junk Publ.

Sasano, Y., Nakane H. (1984): Significance of the extinction/backscatter ratio and the boundary value term in the solution for the two-component lidar equation. Appl. Opt., 23, 11–13.

Schaaf, C.L.B., Liu, J., Gao, F. Strahler, A.H. (2011): MODIS Albedo and Reflectance Anisotropy Products from Aqua and Terra, In Land Remote Sensing and Global Environmental Change: NASA's Earth Observing System and the Science of ASTER and MODIS, Remote Sensing and Digital Image Processing Series, 11, B. Ramachandran, C. Justice, M. Abrams, Eds, Springer-Cerlag, 873.

Sorribas, M., Ogren, J. A., Olmo, F. J., Quirantes, A., Fraile, R., Gil-Ojeda, M., Alados-Arboledas, L. (2015): Assessment of African desert dust episodes over the southwest Spain at sea level using in situ aerosol optical and microphysical properties. Tellus B, 67, 1, 27482.

Stein, A.F., Draxler, R.R., Rolph, G.D., Stunder, B.J., Cohen, M.D., Ngan, F. (2015): NOAA’s HYSPLIT atmospheric transport and dispersion modeling system. Bull. Am. Meteorol Soc., 96, 12, 2059-2077.

Tesche, M., Ansmann, A., Müller, D., Althausen, D., Mattis, I. N. A., Heese, B., Freudenthaler, V., Wiegner, M., Esselborn, M., Pisani, G., Knippertz, P. (2009): Vertical profiling of Saharan dust with Raman lidars and airborne HSRL in southern Morocco during SAMUM. Tellus B, 61, 1, 144-164.

Tesche, M., Gross, S., Ansmann, A., Müller, D., Althausen, D., Freudenthaler, V., Esselborn, M. (2011): Profiling of Saharan dust and biomass- burning smoke with multiwavelength polarization Raman lidar at Cape Verde. Tellus B, 6, 4, 649-676.

Titos G, Foyo-Moreno I, Lyamani H, Querol X, Alastuey A, Alados-Arboledas L. (2012): Optical properties and chemical composition of aerosol particles at an urban location: An estimation of the aerosol mass scattering and absorption efficiencies, J. Geophys. Res., 117, D04206, doi:10.1029/2011JD016671.

Titos G., Lyamani H., Pandolfi M., Alastuey A., Alados-Arboledas L. (2014): Identification of fine (PM1) and coarse (PM10-1) sources of particulate matter in an urban environment. Atmos. Environ., 89, 593-602.

Torres, B., Dubovik, O., Fuertes, D., Lapyonok, T., Toledano, C., Schuster, G. L., Goloub, P., Blarel, L., Barreto, A., Mallet, M., Tanré, D. (2017): Advanced characterization of aerosol properties from measurements of spectral optical depth using the GRASP algorithm. Atmos. Meas. Tech., 10, 3743-3781, doi: 10.5194/amt-10-3743-2017.

Valenzuela, A., Olmo, F.J., Lyamani, H., Antón, M., Quirantes, A., Alados-Arboledas, L. (2012): Aerosol radiative forcing during African desert dust events (2005–2010) over Southeastern Spain. Atmos. Chem. Phys., 12, 21, 10331-10351.

Veselovskii, I., Kolgotin, A., Griaznov, V., Müller, D., Wandinger, U., Whiteman, D. N. (2002): Inversion with regularization for the retrieval of tropospheric aerosol parameters from multiwavelength lidar sounding, Appl. Opt., 41, 3685–3699, doi:10.1364/AO.41.003685.

Veselovskii, I., Whiteman, D.N., Korenskiy, M., Kolgotin, A., Dubovik, O., Perez-Ramirez, D., Suvorina, A. (2013): Retrieval of spatio-temporal distributions of particle parameters from multiwavelength lidar measurements using the linear estimation technique and comparison with AERONET. Atmos. Meas. Tech., 6, 2671-2682.

Veselovskii, I., Whiteman, D.N., Korenskiy, M., Suvorina, A., Kolgotin, A., Lyapustin, A., Wang, Y., Chin, M., Bian, H., Kucsera, T.L., Pérez-Ramírez, D., Holben, B. (2015): Characterization of forest fire smoke event near Washington, DC in summer 2013 with multi-wavelength lidar. Atmos. Chem. Phys., 15, 1647-1660.

Veselovskii, I., Goloub, P., Podvin, T., Tanre, D., da Silva, A., Colarco, P., Castellanos, P., Korenskiy, M., Hu, Q., Whiteman, D.N., Perez-Ramirez, D., Augustin, P., Fourmentin, M., and Kolgotin, A. (2017): Characterization of smoke/dust episode over West Africa: comparison of MERRA-2 modeling with multiwavelength Mie-Raman lidar observations. Atmos. Meas. Tech. Discuss., doi:10.5194/amt-2017-342.

Wandinger, U., Müller, D., Bockman, C., Althausen, D., Matthias, V., Bosenberg, J., WeiB, V., Fiebig, M., Wendisch, M., Stohl, A., Ansmann, A. (2002): Optical and microphysical characterization of biomass- burning and industrial-pollution aerosols from multiwavelength lidar and aircraft measurements. Journal of Geophys. Res., 107, D21, 8125, doi:10.1029/2000JD000202.

Whiteman, D.N., Melfi, S.H., and Ferrare, R.A. (1992): Raman lidar system for the measurement of water vapor and aerosol in the Earth's atmosphere. Appl. Opt., 31, 3061-3082, doi.org/10.1364/AO.31.003068.

Wiedensohler, A., Birmili, W., Nowak, A., Sonntag, A., Weinhold,K., Merkel, M., Wehner, B., Tuch, T., Pfeifer, S., Fiebig, M.,Fjäraa, A. M., Asmi, E., Sellegri, K., Depuy, R., Venzac, H., Villani,P., Laj, P., Aalto, P., Ogren, J. A., Swietlicki, E., Williams,P., Roldin, P., Quincey, P., Hüglin, C., Fierz-Schmidhauser, R.,Gysel, M., Weingartner, E., Riccobono, F., Santos, S., Grüning,C., Faloon, K., Beddows, D., Harrison, R., Monahan, C., Jennings,S. G., O'Dowd, C. D., Marinoni, A., Horn, H.-G., Keck,L., Jiang, J., Scheckman, J., McMurry, P. H., Deng, Z., Zhao, C.S., Moerman, M., Henzing, B., de Leeuw, G., Löschau, G., Bastian, S. (2012): Mobility particle size spectrometers: harmonizationof technical standards and data structure to facilitate high quality long-term observations of atmospheric particle number sized distributions. Atmos. Meas. Tech., 5, 657–685, doi:10.5194/amt-5-657-2012.

Wiegner, M., Geiss, A. (2012): Aerosol profiling with the Jenoptik ceilometer CHM15kx. Atmos. Meas. Tech., 5, 8, 1953-1964, doi:10.5194/amt-5-1953-2012.

Wiegner, M., Madonna, F., Binietoglou, I., Forkel, R., Gasteiger, J., Geiß, A., Pappalardo, G., Schäfer, K., Thomas, W. (2014): What is the benefit of ceilometers for aerosol remote sensing? An answer from EARLINET. Atmos. Meas. Tech., 7, 1979-1997.

Figures

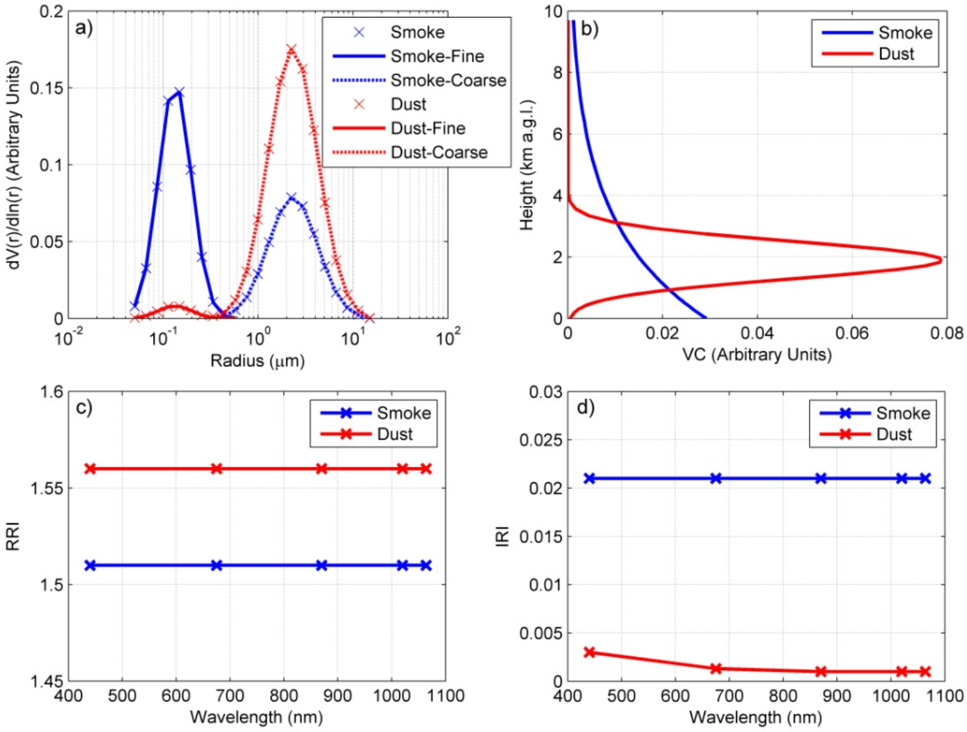

Figure 1: Microphysical and optical properties of the two aerosol models (Smoke and Dust) used to obtain synthetic data: size distribution (panel a); vertical volume concentration, VC, (panel b); real (panel c) and imaginary (panel d) refractive indices, RRI and IRI, respectively.

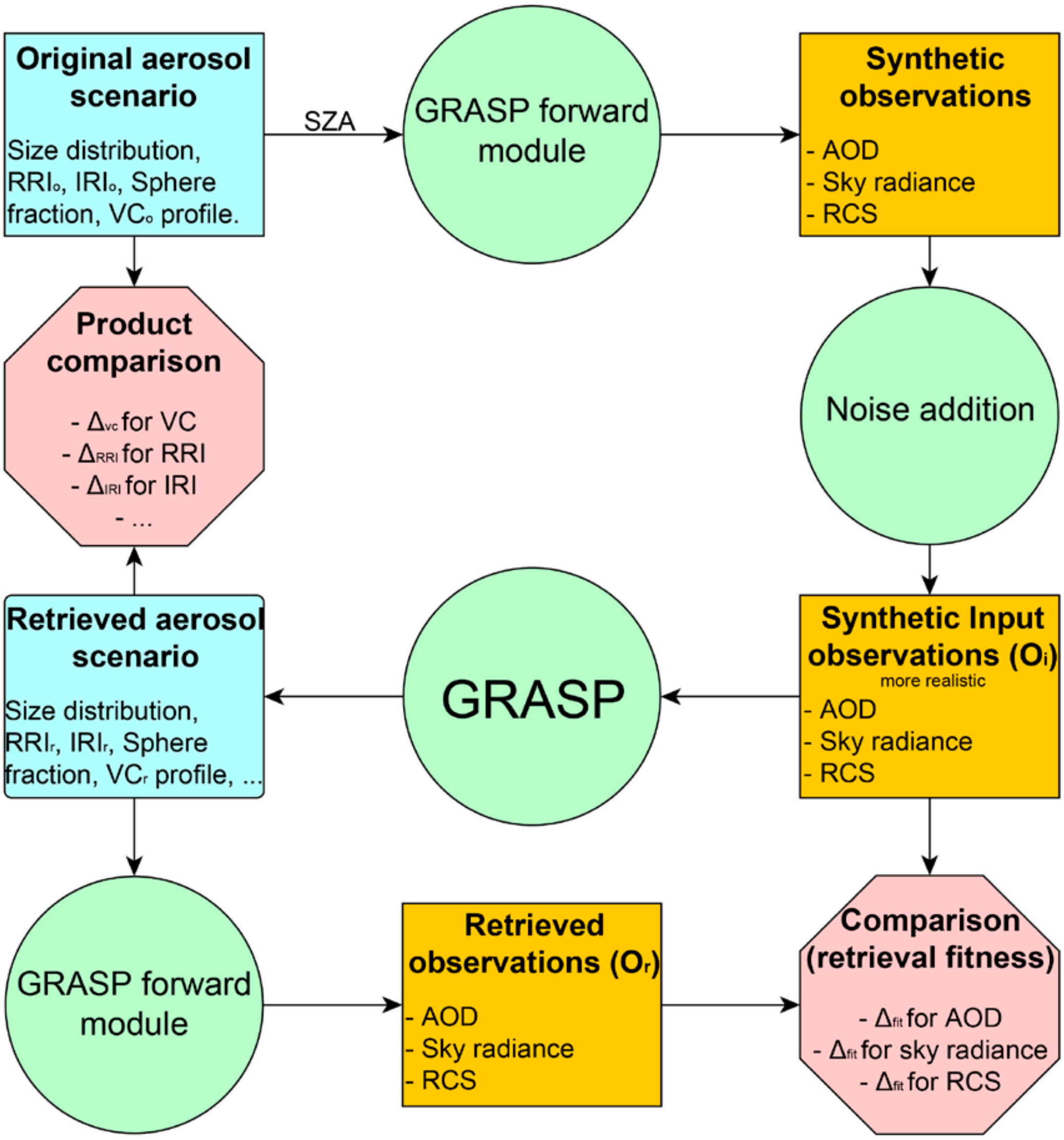

Figure 2: Flow diagram about retrieval sensitivity study with synthetic data.

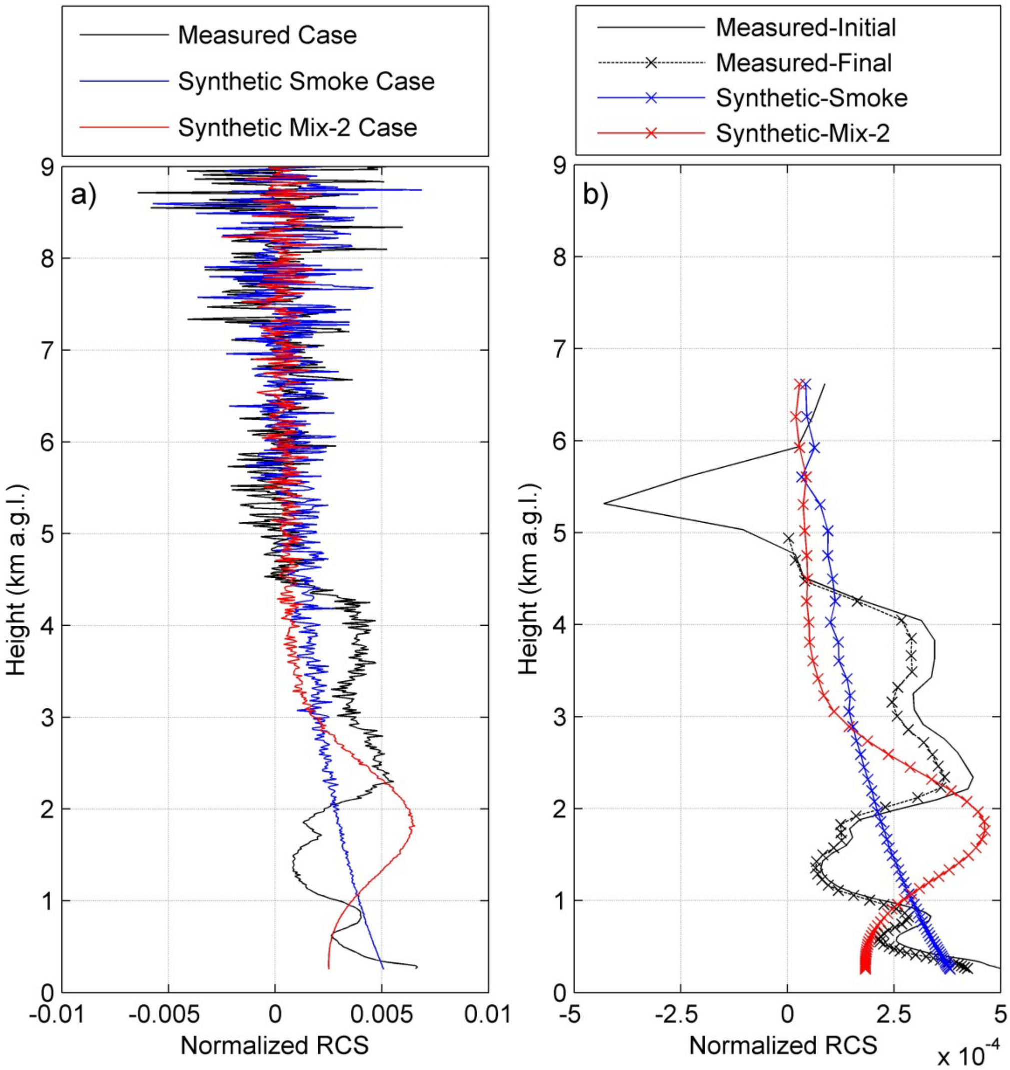

Figure 3: Range corrected signals (RCS) at 1064 nm, from 250 m to 9000 m every 15 m, normalized by the sum of all data (panel a) for three cases: half hour average of measured ceilometer signal on 17 June 2013, 07:40 UTC (AOD_{440}~0.21) (black line); synthetic and noisy signal of Smoke with AOD_{440} equal to 0.4 (blue line); and synthetic and noisy signal of "Mix-2" with AOD_{440} equal to 0.4 (red line). Panel b shows the RCS of panel a, but normalized to 60 log-spaced points following the criteria used for $GRASP_{pac}$.

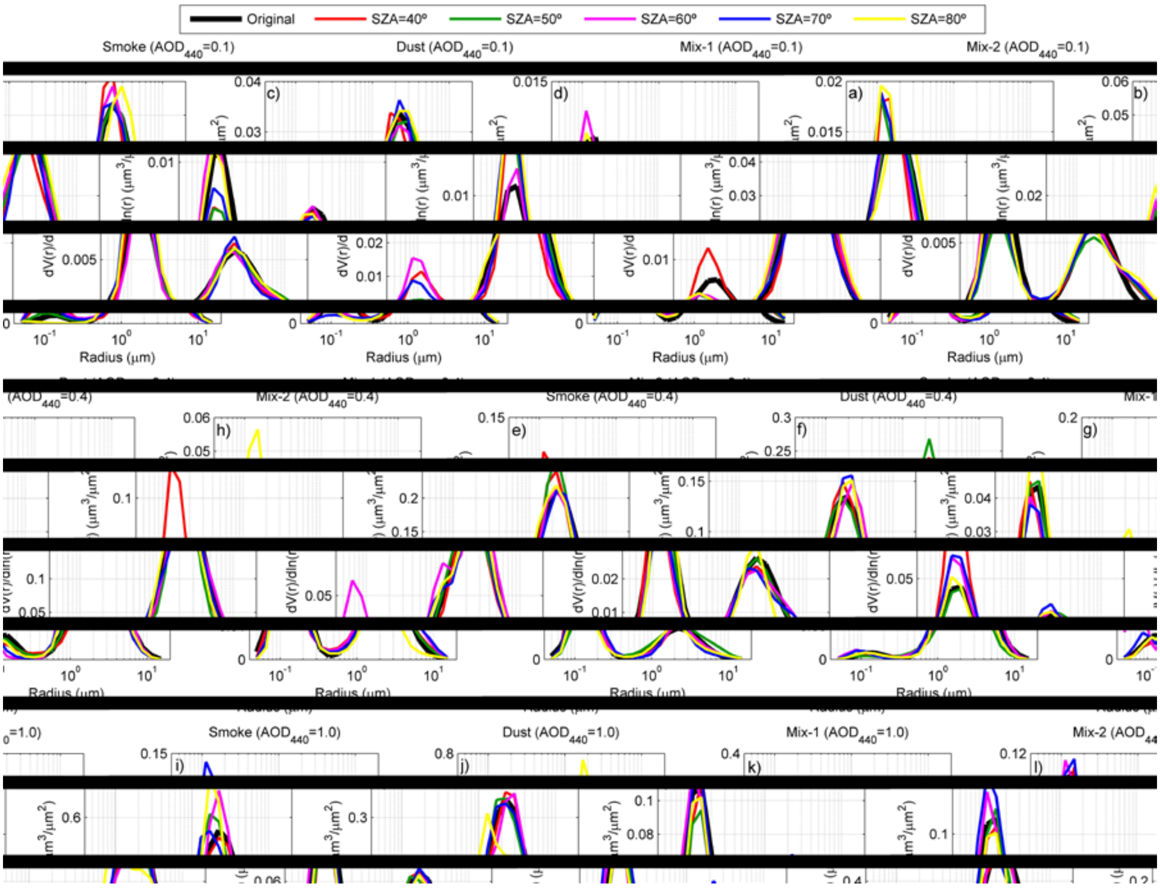

Figure 4: Original aerosol size distribution as retrieved by GRASP$_{pac}$ for different aerosol types (Smoke, Dust, Mix-1 and Mix-2) and loads (AOD_{440}=0.1, 0.4 and 1.0), and at different solar zenith angles (SZA) from 40º to 80º.

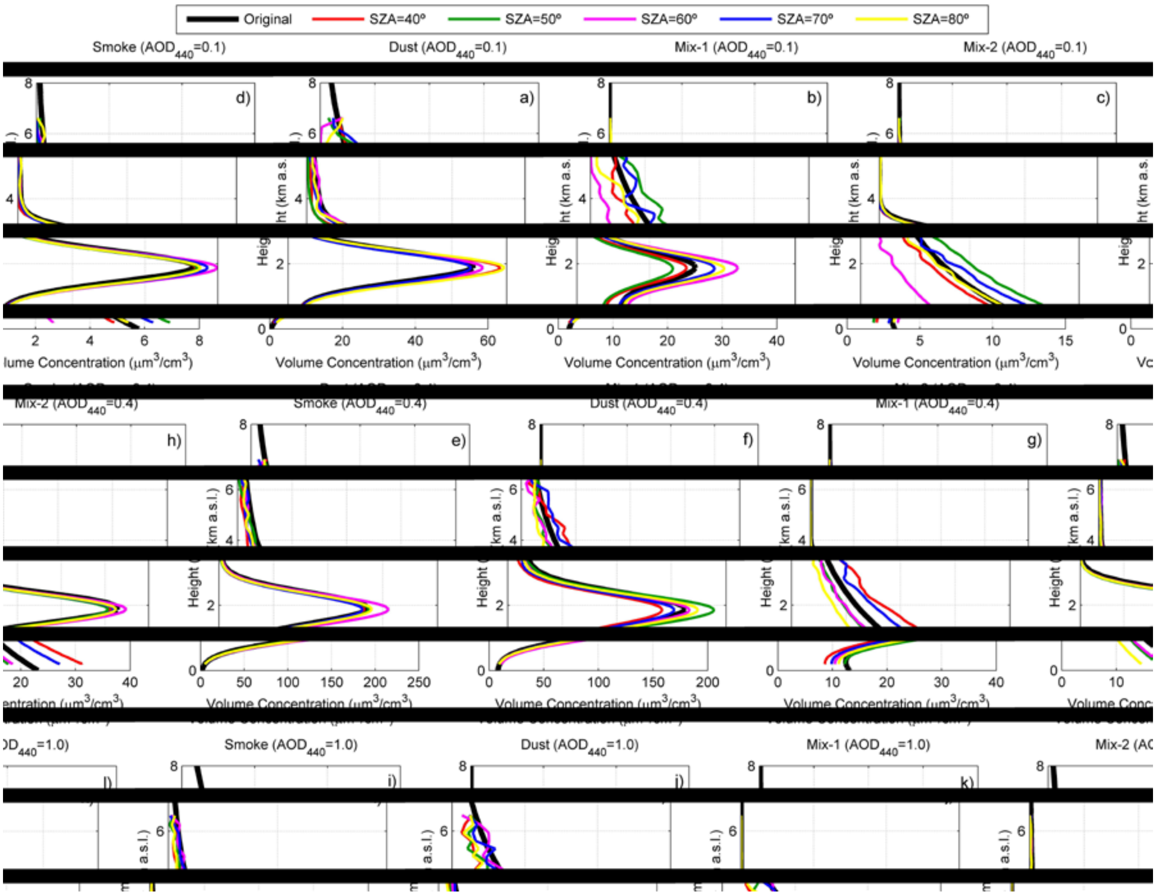

Figure 5: Original aerosol volume concentration (VC) vertical profile as retrieved by $GRASP_{pac}$ for different aerosol types (Smoke, Dust, Mix-1 and Mix-2) and loads (AOD_{440}=0.1, 0.4 and 1.0), and at different solar zenith angles (SZA) from 40º to 80º.

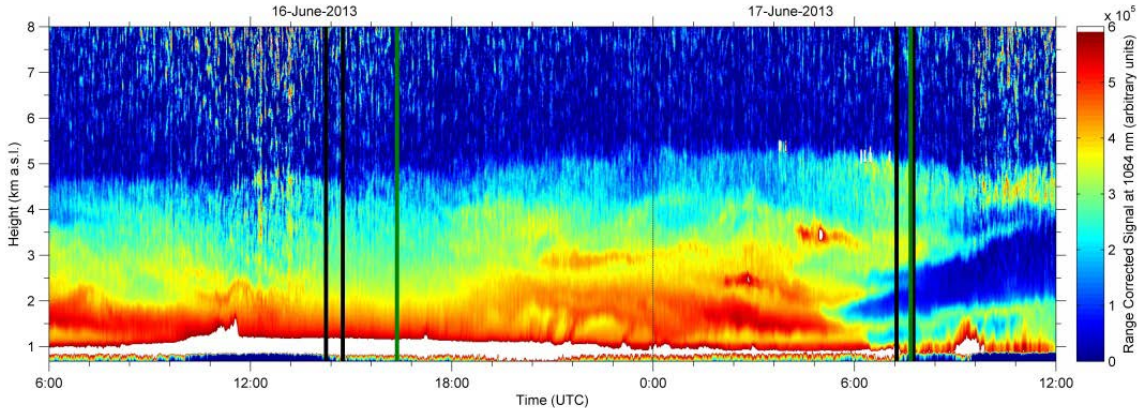

Figure 6: Ceilometer range corrected signal at 1064 nm as a function of height and time from 16th, 6 UTC, to 17th June, 12 UTC, 2013. White colour represents all values above 6E5 arbitrary units. The times between vertical black lines corresponds to the F30 and F31 flights. Green vertical lines corresponds in time with the sky radiance and AOD measurements (sun photometer) nearest to the flights.

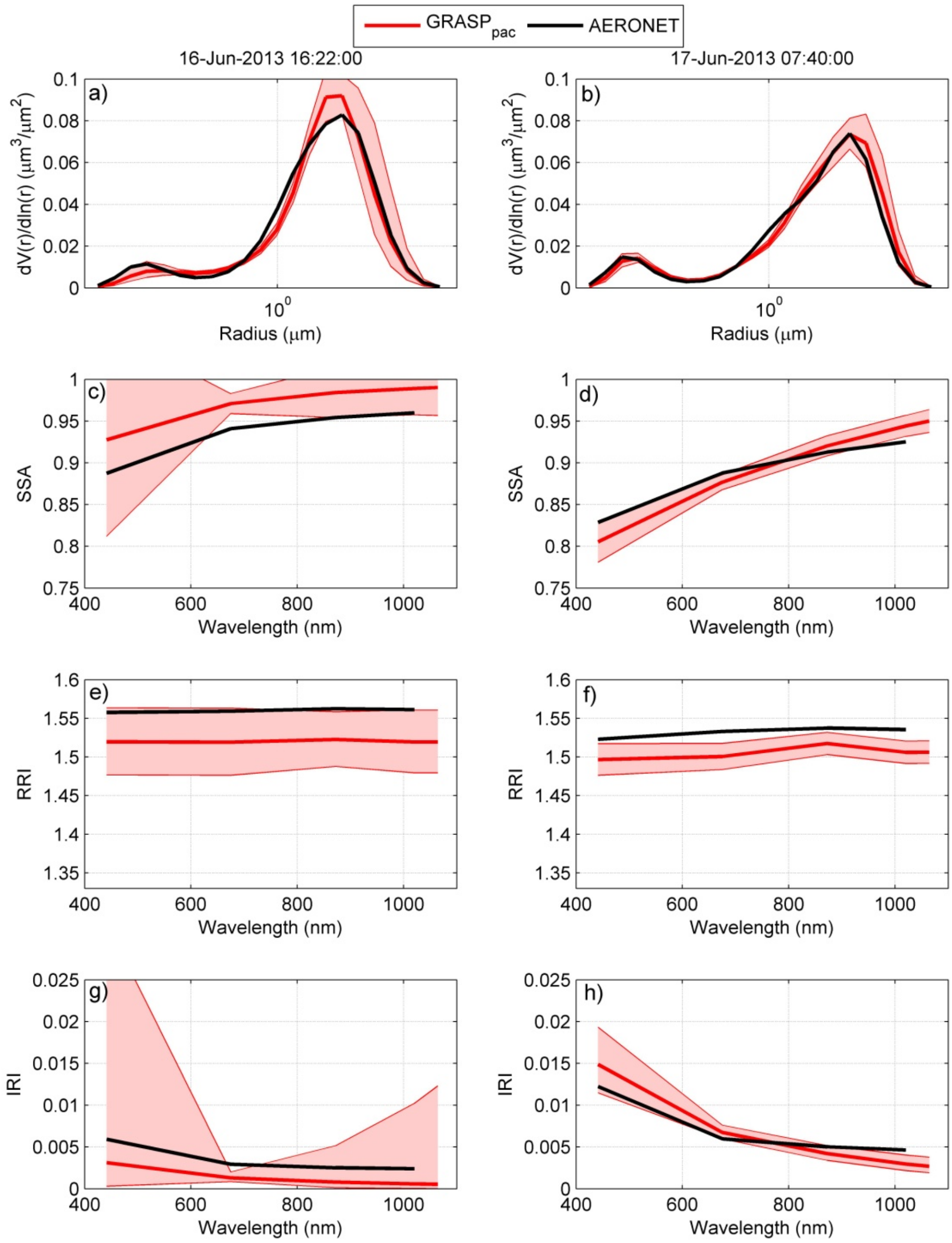

Figure 7: Columnar size distribution (panels a and b), single scattering albedo (SSA; panels c and d), real refractive index (RRI, panels e and f) and imaginary refractive index (IRI; panels g and h) obtained by AERONET (black line) and GRASP (red line) at 16 June 2013 16:22 UTC (left panels) and 17 June 2013 07:40 UTC (right panels). Shadow band represents uncertainty in the $GRASP_{pac}$ retrieval.

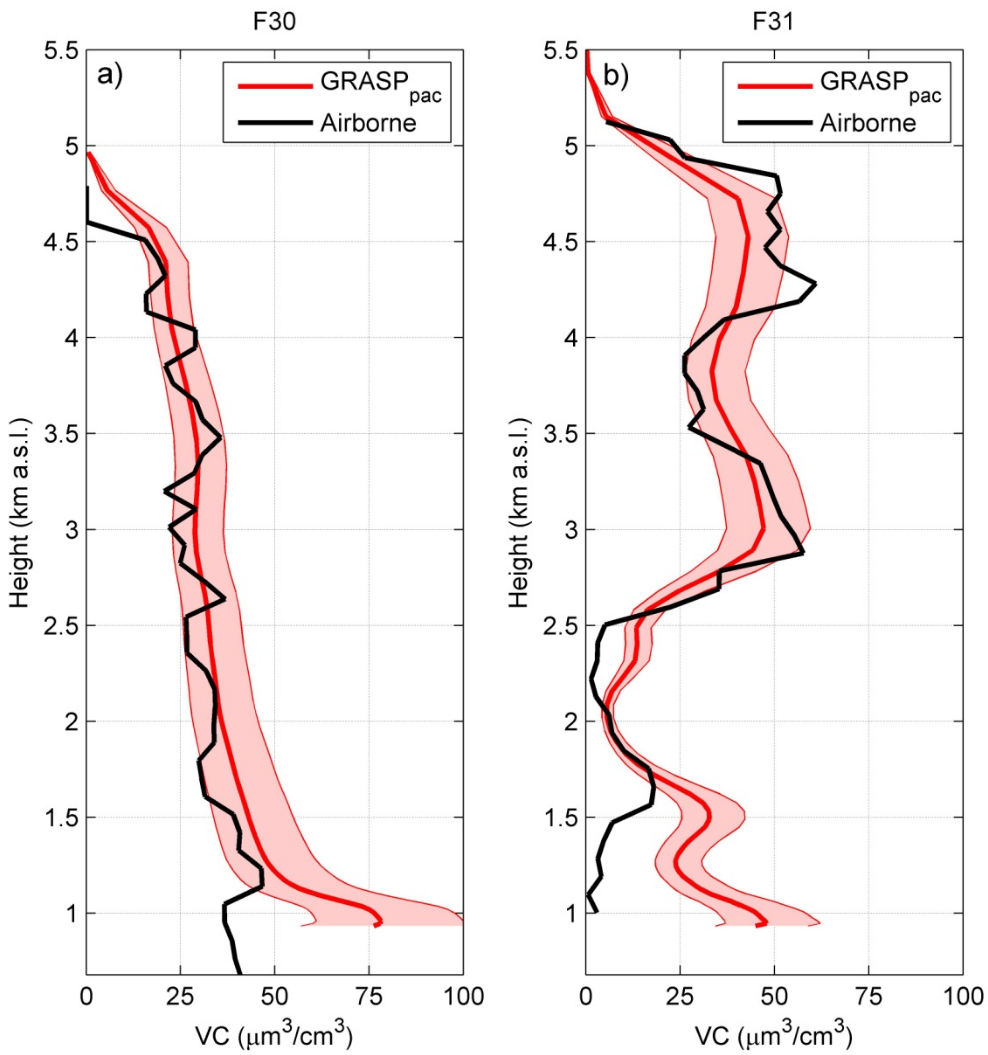

Figure 8: Profiles of aerosol volume concentration (VC) obtained by airborne instrumentation (black line) and $GRASP_{pac}$ (red line) at the flights F30 (panel a) and F31 (panel b). Shadow band represents uncertainty in the $GRASP_{pac}$ retrieval.

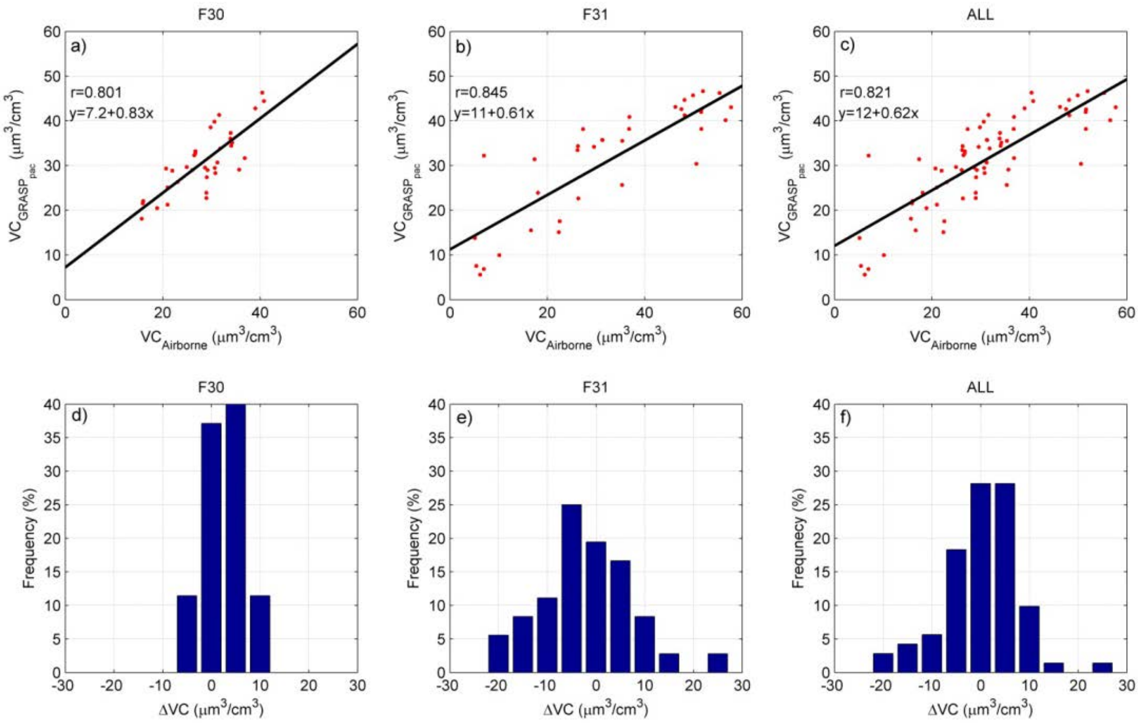

Figure 9: Aerosol volume concentration (VC) retrieved by $GRASP_{pac}$ as a function of the airborne measurements for the flights F30 (panel a), F31 (panel b) and all (panel c). Histograms of the differences between the VC retrieved by GRASP and the VC from airborne (ΔVC from Eq. (10)) for the flights F30 (panel d), F31 (panel e) and all (panel f).

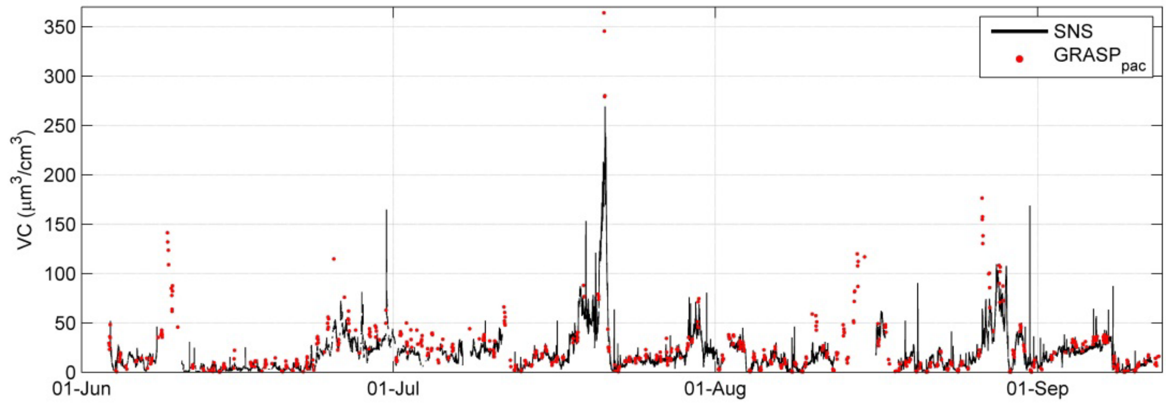

Figure 10: Temporal evolution of the aerosol volume concentration (VC) measured at the Sierra Nevada Station (SNS) and the retrieved by $GRASP_{pac}$ at the same altitude.

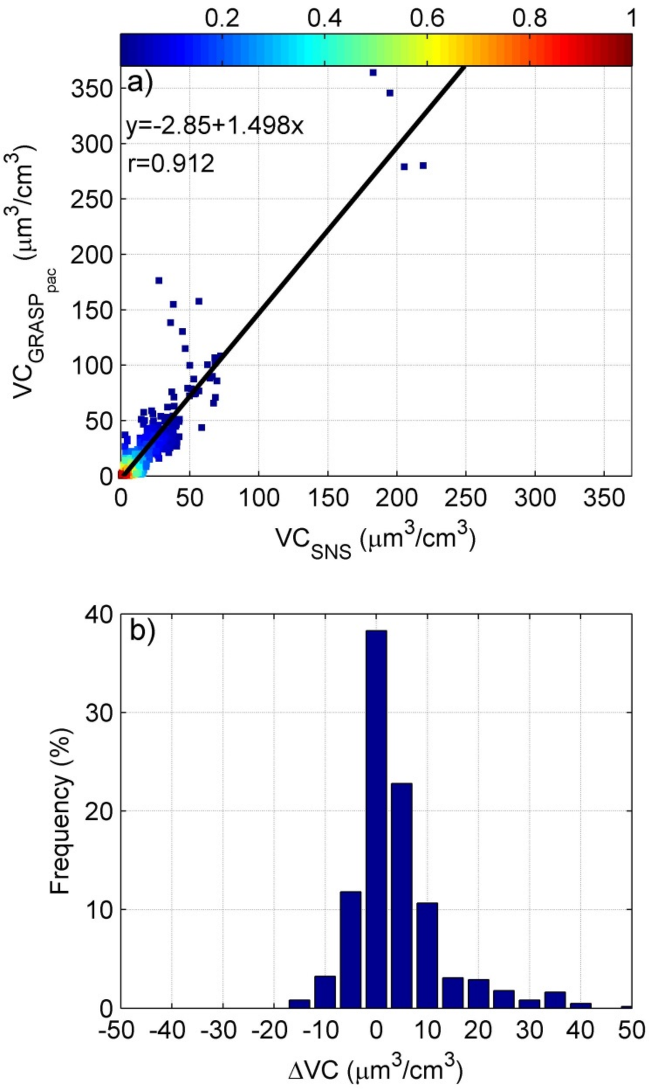

Figure 11: Aerosol volume concentration (VC) retrieved by $GRASP_{pac}$ at the Sierra Nevada Station (SNS) altitude as a function of the VC directly measured at SNS (panel a). Colour of points represents the relative density of the points. Histograms of the differences (ΔVC from Eq. (12)) between the VC retrieved by $GRASP_{pac}$ at SNS altitude and the VC directly measured at SNS (panel b).

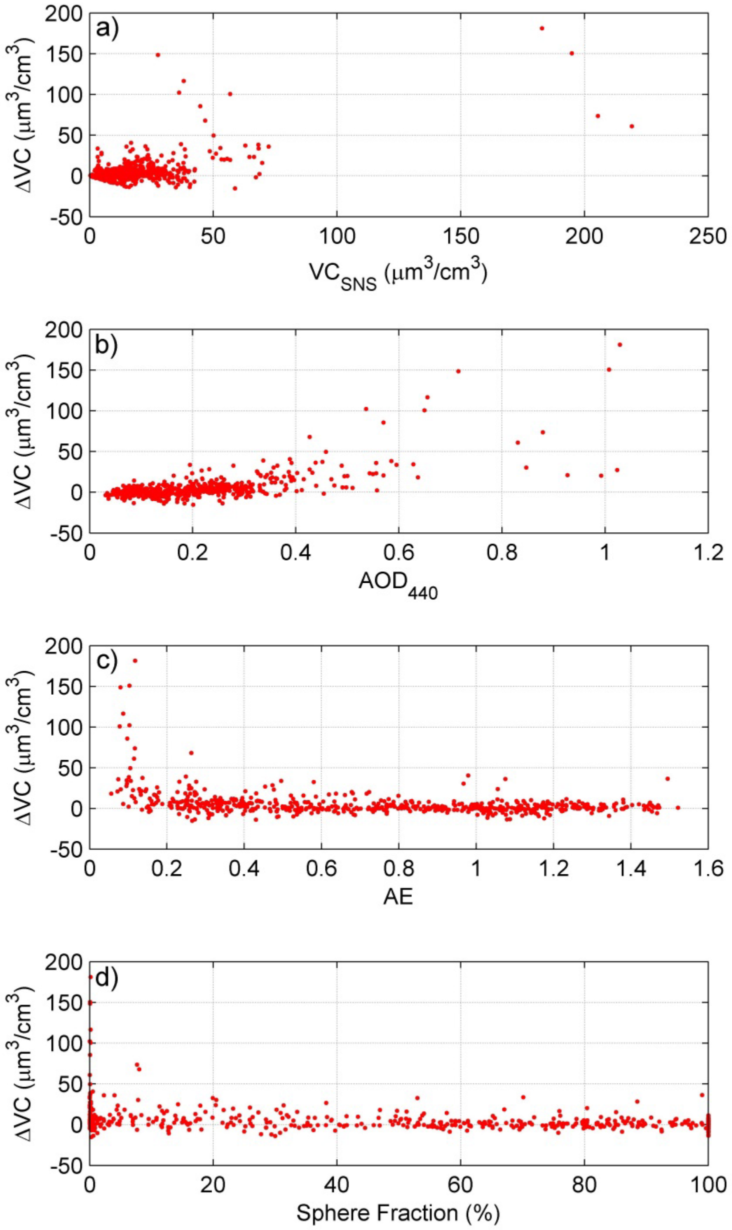

Figure 12: Differences between the aerosol volume concentration (VC) retrieved by GRASP$_{pac}$ at Sierra Nevada Station (SNS) altitude and the VC directly measured at SNS (ΔVC from Eq. (12)) as a function of the VC at SNS (panel a), aerosol optical depth at 440 nm (panel b), Angström Exponent (panel c) and sphere fraction (panel d).

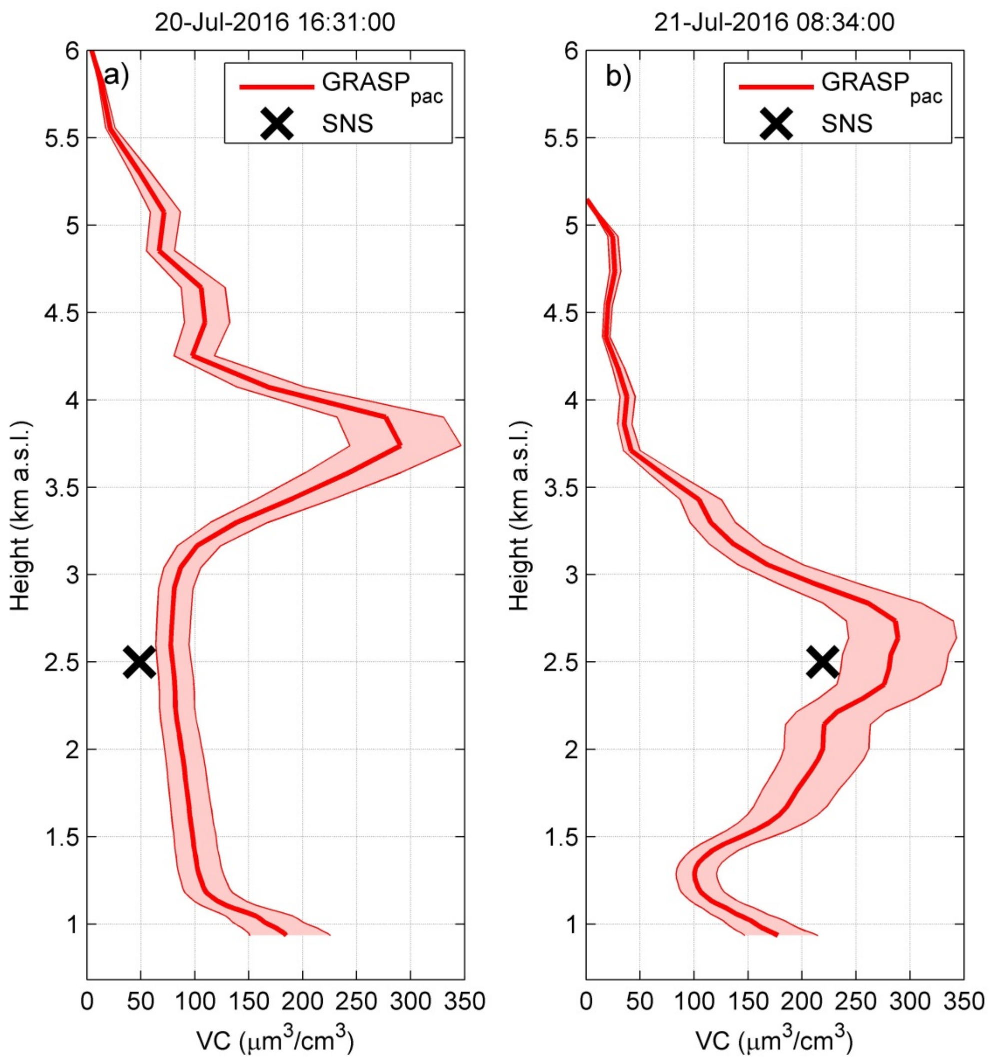

Figure 13: Profiles of aerosol volume concentration (VC) retrieved by GRASP$_{pac}$ at 20 July 2016, 18:12 UTC (panel a) and 21 July 2016, 09:32 UTC (panel b). VC measured at Sierra Nevada Station (SNS) is marked by a black cross. Shadow band represents uncertainty in the GRASP$_{pac}$ retrieval.

Tables

Table 1: Mean bias error (MBE) of the $GRASP_{pac}$ retrievals (Δ_{fit} from Eq. (6) and (7)) of AOD, sky radiance, and lidar range-corrected signal (aod, rad, and rcs respective index) under different aerosol scenarios. Standard deviation (STD) of Δ_{fit} is in parenthesis.

Aerosol Type*	SZA (°)	Scattering Angle Range (°)	AOD_{440}=0.1			AOD_{440}=0.4			AOD_{440}=1.0		
			MBE_{aod} (x1000)	MBE_{rad} (%)	MBE_{rcs} (%)	MBE_{aod} (x1000)	MBE_{rad} (%)	MBE_{rcs} (%)	MBE_{aod} (x1000)	MBE_{rad} (%)	MBE_{rcs} (%)
Smoke	40	2.3-78.6	5.3 (8.2)	-0.5 (3.0)	0.0 (1.3)	1.8 (3.0)	-0.1 (3.1)	0.2 (4.7)	-0.3 (0.4)	-0.2 (2.8)	0.1 (1.3)
	50	2.7-98.0	16.7 (19.7)	-0.3 (2.7)	0.4 (5.3)	-1.5 (3.0)	0.2 (2.9)	0.0 (0.4)	1.0 (1.5)	-0.5 (3.8)	0.2 (2.3)
	60	3.0-117.1	0.5 (0.7)	-0.1 (3.1)	0.1 (3.1)	0.4 (0.4)	-0.1 (2.8)	0.1 (1.6)	13.5 (17.4)	-1.7 (3.6)	-0.1 (2.7)
	70	3.3-135.5	3.8 (5.8)	-0.6 (3.0)	0.0 (2.0)	-1.1 (2.0)	-0.5 (3.6)	0.2 (3.4)	0.4 (0.2)	-0.1 (3.2)	0.1 (0.9)
	80	3.5-151.8	2.6 (3.7)	-0.6 (2.8)	0.1 (2.3)	1.7 (3.5)	-1.3 (3.0)	0.2 (0.7)	-0.1 (0.8)	-0.3 (3.3)	0.2 (2.5)
Dust	40	2.3-78.6	16.7 (30.4)	-2.9 (4.0)	7.2 (14.7)	-5.5 (8.6)	-1.1 (2.9)	0.5 (4.1)	9.4 (7.7)	-3.2 (4.0)	0.3 (2.6)
	50	2.7-98.0	3.2 (4.2)	-0.8 (3.0)	1.9 (5.4)	-5.1 (7.4)	0.8 (4.4)	0.1 (4.2)	11.6 (11.3)	1.5 (4.5)	1.3 (4.8)
	60	3.0-117.1	16.5 (31.3)	-0.2 (3.2)	0.7 (5.0)	-2.9 (4.7)	0.0 (3.3)	0.0 (2.3)	-3.0 (4.9)	1.1 (4.0)	0.5 (1.9)
	70	3.3-135.5	7.5 (14.3)	-0.6 (3.0)	0.3 (3.7)	-3.7 (6.5)	0.7 (3.4)	0.0 (1.7)	8.7 (6.2)	0.3 (3.6)	0.2 (2.9)
	80	3.5-151.8	-4.0 (7.5)	0.7 (3.2)	0.3 (1.1)	7.6 (10.3)	-0.3 (2.7)	0.2 (2.0)	3.6 (4.0)	0.2 (3.4)	0.2 (1.9)
Mix-1	40	2.3-78.6	4.1 (6.3)	-0.5 (2.8)	0.9 (3.1)	-3.0 (4.0)	-0.5 (3.4)	0.4 (1.7)	-5.9 (10.4)	0.1 (2.9)	-0.2 (1.9)
	50	2.7-98.0	-7.6 (13.5)	0.1 (3.6)	0.9 (2.3)	11.2 (16.7)	0.1 (3.3)	0.3 (6.8)	-0.4 (0.8)	0.2 (3.6)	-0.1 (2.8)
	60	3.0-117.1	-5.6 (7.6)	2.4 (5.6)	8.4 (11.8)	-2.1 (4.5)	2.3 (7.0)	0.0 (2.0)	-1.0 (1.3)	0.6 (3.1)	-0.2 (1.5)
	70	3.3-135.5	-2.8 (4.3)	0.4 (3.4)	1.2 (4.1)	-8.4 (16.4)	2.1 (4.7)	0.6 (2.7)	1.9 (3.0)	0.5 (3.4)	0.1 (1.1)
	80	3.5-151.8	-2.8 (8.0)	6.4 (8.0)	8.1 (11.1)	-2.2 (3.0)	1.7 (3.8)	-0.2 (1.6)	9.3 (12.5)	1.5 (4.6)	0.4 (3.9)
Mix-2	40	2.3-78.6	-3.3 (6.7)	-1.8 (3.5)	1.4 (5.1)	2.4 (3.7)	1.3 (5.1)	0.8 (8.3)	-0.1 (0.2)	-0.2 (3.3)	0.0 (1.1)
	50	2.7-98.0	-3.8 (6.0)	-2.0 (3.2)	1.1 (6.0)	0.7 (1.1)	-0.4 (3.1)	0.1 (2.0)	0.4 (1.2)	0.0 (2.9)	0.1 (5.4)
	60	3.0-117.1	1.1 (2.5)	-0.2 (3.4)	0.6 (3.6)	1.6 (2.6)	1.4 (4.9)	0.4 (3.2)	0.0 (0.4)	1.0 (3.5)	0.0 (0.9)
	70	3.3-135.5	1.9 (4.9)	-3.5 (4.4)	2.1 (9.7)	-0.4 (1.0)	-0.1 (2.6)	0.0 (1.0)	-0.8 (0.5)	0.1 (3.3)	0.0 (0.3)
	80	3.5-151.8	-0.7 (0.9)	-0.1 (2.5)	0.1 (2.6)	0.0 (1.1)	0.0 (3.5)	0.1 (1.4)	0.1 (0.1)	0.1 (2.4)	0.0 (1.4)

*See section 4.1 for the aerosol models description.

Table 2: MBE and STD from the differences between the VC retrieved by GRASP$_{pac}$ and the original VC (Δ_{vc} from Eq. (8) and (9)) under different aerosol scenarios and SZA values. Original VC values below 1 $\mu m^3/cm^3$ have not been taken into account in the calculations. MBE and STD are given in % in parenthesis.

Aerosol Type*	SZA (º)	AOD$_{440}$=0.1		AOD$_{440}$=0.4		AOD$_{440}$=1.0		All	
		MBE ($\mu m^3/cm^3$)	STD ($\mu m^3/cm^3$)	MBE ($\mu m^3/cm^3$)	STD ($\mu m^3/cm^3$)	MBE ($\mu m^3/cm^3$)	STD ($\mu m^3/cm^3$)	MBE ($\mu m^3/cm^3$)	STD ($\mu m^3/cm^3$)
Smoke	40	-0.5 (-15.5)	0.1 (8.4)	6.0 (39.2)	3.2 (17.1)	-12.7 (-38.2)	4.8 (6.5)	-2.5 (-4.5)	8.5 (35.0)
	50	1.2 (33.6)	0.3 (5.9)	-2.5 (-18.6)	1.0 (5.7)	-8.7 (-26.4)	3.2 (6.9)	-3.5 (-4.9)	4.5 (27.1)
	60	-2.0 (-57.9)	0.5 (9.4)	-2.2 (-18.7)	0.7 (11.0)	-0.5 (-1.8)	0.8 (9.0)	-1.6 (-25.2)	1.0 (25.2)
	70	0.6 (14.9)	0.3 (9.8)	3.6 (24.8)	1.8 (13.3)	0.6 (-0.7)	1.4 (8.4)	1.6 (12.9)	2.0 (15.1)
	80	-0.1 (-6.1)	0.2 (11.8)	-4.6 (-33.6)	1.8 (5.8)	-8.9 (-27.5)	3.1 (6.9)	-4.7 (-22.9)	4.2 (14.4)
	All	-0.2 (-6.2)	1.1 (32.3)	0.0 (-1.4)	4.4 (30.4)	-6.0 (-18.9)	6.0 (16.8)	-2.1 (-8.9)	5.2 (28.2)
Dust	40	0.3 (-1.5)	1.7 (13.1)	-2.0 (-2.7)	6.7 (12.4)	-3.1 (-1.4)	14.0 (11.3)	-1.6 (-1.9)	9.2 (12.2)
	50	0.5 (3.6)	1.6 (10.6)	-3.1 (-5.2)	7.2 (13.8)	-9.0 (-5.7)	16.2 (11.6)	-4.0 (-2.6)	11.1 (12.7)
	60	2.2 (11.5)	2.7 (10.9)	3.6 (5.4)	6.9 (12.7)	-1.9 (-1.5)	14.3 (12.5)	1.3 (5.0)	9.6 (13.1)
	70	1.3 (5.8)	2.1 (11.0)	-0.5 (2.1)	6.5 (12.1)	-10.1 (-7.2)	15.5 (11.4)	-3.2 (0.1)	11.1 (12.7)
	80	1.1 (15.5)	1.7 (18.2)	-0.3 (-1.0)	5.7 (11.8)	-20.1 (-11.8)	25.0 (10.9)	-6.6 (0.6)	17.8 (17.8)
	All	1.1 (7.0)	2.1 (14.3)	-0.5 (-0.3)	6.9 (13.0)	-8.8 (-5.5)	18.5 (12.1)	-2.8 (0.3)	12.4 (14.1)
Mix-1	40	1.4 (1.8)	2.1 (18.1)	-1.1 (-8.9)	3.4 (14.0)	0.9 (-6.1)	7.1 (13.9)	0.3 (-4.8)	4.9 (15.8)
	50	-0.1 (-1.5)	0.9 (8.2)	0.1 (-6.8)	3.3 (12.5)	-0.7 (-7.0)	7.9 (12.5)	-0.3 (-5.3)	5.1 (11.6)
	60	0.6 (2.1)	1.1 (9.3)	6.1 (18.6)	7.3 (17.9)	-5.0 (-9.7)	9.7 (12.1)	0.5 (3.7)	8.6 (18.2)
	70	-0.2 (-3.1)	0.9 (8.6)	-1.1 (-1.1)	3.7 (13.1)	-3.0 (-10.6)	8.8 (14.2)	-1.5 (-5.1)	5.8 (13.0)
	80	2.0 (14.9)	2.1 (8.7)	1.0 (-2.7)	3.5 (13.0)	-2.3 (-10.7)	6.0 (14.8)	0.1 (-0.4)	4.7 (16.3)
	All	0.7 (2.9)	1.8 (12.8)	1.0 (-0.2)	5.2 (17.2)	-2.0 (-8.8)	8.2 (13.6)	-0.2 (-2.4)	6.0 (15.6)
Mix-2	40	-0.8 (-24.5)	0.2 (13.2)	-3.1 (-28.2)	1.1 (14.1)	-6.7 (-23.7)	2.7 (11.3)	-3.7 (-25.6)	3.0 (13.0)
	50	-1.2 (-32.2)	0.2 (10.9)	1.2 (-1.2)	2.0 (21.4)	-4.6 (-18.0)	1.9 (12.1)	-1.6 (-16.1)	3.0 (20.1)
	60	1.1 (21.9)	0.9 (12.3)	-0.9 (-12.5)	1.0 (12.8)	0.4 (-3.2)	3.3 (12.6)	0.2 (0.8)	2.3 (18.9)
	70	0.3 (2.7)	0.6 (10.2)	-1.9 (-18.5)	0.8 (12.4)	0.2 (-4.2)	3.3 (12.7)	-0.5 (-7.3)	2.3 (14.7)
	80	0.7 (11.1)	0.7 (12.6)	-0.2 (-8.6)	1.3 (14.8)	-10.1 (-32.0)	4.8 (9.5)	-3.5 (-11.2)	5.8 (21.4)
	All	0.0 (-4.2)	1.1 (23.9)	-1.0 (-13.8)	2.0 (17.8)	-4.2 (-16.2)	5.2 (16.1)	-1.8 (-11.9)	3.8 (19.9)
All	40	0.1 (-10.1)	1.6 (17.1)	0.0 (0.0)	5.4 (29.1)	-5.5 (-18.0)	9.4 (18.3)	-1.9 (-9.4)	7.0 (23.5)
	50	0.1 (1.9)	1.3 (25.4)	-1.0 (-8.1)	4.3 (15.8)	-5.6 (-14.6)	9.4 (13.8)	-2.3 (-7.3)	6.6 (19.8)
	60	0.4 (-7.3)	2.2 (33.6)	1.6 (-2.2)	6.0 (20.3)	-1.7 (-4.1)	8.7 (12.0)	0.1 (-4.4)	6.5 (23.2)
	70	0.5 (5.3)	1.3 (11.9)	0.0 (1.8)	4.3 (20.2)	-2.8 (-5.6)	9.6 (12.4)	-0.8 (0.3)	6.4 (16.1)
	80	0.9 (8.4)	1.6 (15.9)	-1.1 (-12.0)	4.0 (17.7)	-10.0 (-20.8)	13.9 (14.4)	-3.6 (-8.9)	9.8 (20.0)
	All	0.4 (-0.4)	1.6 (23.3)	-0.1 (-4.1)	4.9 (21.7)	-5.1 (-12.6)	10.7 (15.8)	-1.7 (-5.9)	7.5 (21.0)

*See section 4.1 for the aerosol models description.

Table 3: Percentage of differences between the VC retrieved by $GRASP_{pac}$ and the original VC (Δ_{vc} from Eq. (8)) that is below the uncertainty, σ_G, of VC given by $GRASP_{pac}$, for different aerosol scenarios and SZA values. The same percentage but for differences below $2\sigma_G$ is also shown.

Aerosol Type*	SZA (º)	AOD440=0.1		AOD440=0.4		AOD440=1.0		All	
		$\Delta_{VC}<\sigma_G$ (%)	$\Delta_{VC}<2\sigma_G$ (%)	$\Delta_{VC}<\sigma_G$ (%)	$\Delta_{VC}<2\sigma_G$ (%)	$\Delta_{VC}<\sigma_G$ (%)	$\Delta_{VC}<2\sigma_G$ (%)	$\Delta_{VC}<\sigma_G$ (%)	$\Delta_{VC}<2\sigma_G$ (%)
Smoke	40	95.0	100.0	8.3	98.3	1.7	1.7	35.0	66.7
	50	90.0	100.0	88.3	98.3	1.7	85.0	60.0	94.4
	60	1.7	1.7	81.7	93.3	95.0	98.3	59.4	64.4
	70	96.7	100.0	66.7	98.3	93.3	100.0	85.6	99.4
	80	91.7	95.0	3.3	68.3	0.0	85.0	31.7	82.8
	All	75.0	79.3	49.7	91.3	38.3	74.0	54.3	81.6
Dust	40	93.3	100.0	91.7	100.0	93.3	100.0	92.8	100.0
	50	90.0	100.0	80.0	91.7	86.7	98.3	85.6	96.7
	60	86.7	90.0	83.3	95.0	86.7	96.7	85.6	93.9
	70	78.3	85.0	80.0	95.0	85.0	96.7	81.1	92.2
	80	63.3	83.3	86.7	98.3	80.0	90.0	76.7	90.6
	All	82.3	91.7	84.3	96.0	86.3	96.3	84.3	94.7
Mix-1	40	81.7	83.3	85.0	95.0	85.0	98.3	83.9	92.2
	50	100.0	100.0	90.0	100.0	81.7	96.7	90.6	98.9
	60	100.0	100.0	91.7	98.3	80.0	96.7	90.6	98.3
	70	91.7	100.0	88.3	100.0	75.0	93.3	85.0	97.8
	80	98.3	100.0	88.3	100.0	81.7	98.3	89.4	99.4
	All	94.3	96.7	88.7	98.7	80.7	96.7	87.9	97.3
Mix-2	40	55.0	95.0	38.3	80.0	36.7	80.0	43.3	85.0
	50	40.0	90.0	91.7	93.3	61.7	93.3	64.4	92.2
	60	78.3	95.0	88.3	95.0	95.0	98.3	87.2	96.1
	70	95.0	95.0	66.7	86.7	96.7	98.3	86.1	93.3
	80	96.7	98.3	83.3	91.7	1.7	58.3	60.6	82.8
	All	73.0	94.7	73.7	89.3	58.3	85.7	68.3	89.9
All	40	81.3	94.6	55.8	93.3	54.2	70.0	63.7	86.0
	50	80.0	97.5	87.5	95.8	57.9	93.3	75.1	95.6
	60	66.7	71.7	86.3	95.4	89.2	97.5	80.7	88.2
	70	90.4	95.0	75.4	95.0	87.5	97.1	84.4	95.7
	80	87.5	94.2	65.4	89.6	40.8	82.9	64.6	88.9
	All	81.2	90.6	74.1	93.8	65.9	88.2	73.7	90.9

*See section 4.1 for the aerosol models description.

Table 4: Statistical estimators MBE, MABE and STD from ΔVC (Eq. (10)) for the comparison of VC retrieved by $GRASP_{pac}$ and the airborne measured for the F30, F31 and both flights together. Values within parentheses are in % (from Eq. (11)).

Flight	N	MBE ($\mu m^3/cm^3$)	MABE ($\mu m^3/cm^3$)	STD ($\mu m^3/cm^3$)	$\Delta VC<\sigma_G$ (%)	$\Delta VC<2\sigma_G$ (%)
F30	35	2.5 (10.5)	4.1 (15.7)	4.4 (16.5)	77.1	100
F31	36	-1.8 (12.9)	7.5 (33.9)	9.5 (70.8)	58.3	88.9
All	71	0.3 (11.7)	5.8 (24.9)	7.7 (51.4)	67.6	94.4

Table 5: Statistical estimators for the comparison of VC retrieved by $GRASP_{pac}$ and the measured by in-situ instrumentation at SNS (ΔVC from Eq. (12)) along SLOPE I campaign for different VC_{SNS} intervals. Values within parentheses are in % (from Eq. (13)).

VC_{SNS} range	N	MBE ($\mu m^3/cm^3$)	MABE ($\mu m^3/cm^3$)	STD ($\mu m^3/cm^3$)	$\Delta VC<\sigma_G$ (%)	$\Delta VC<2\sigma_G$ (%)
0-Max. $\mu m^3/cm^3$	619	5.5 (31.1)	7.7 (56.0)	16.6 (94.0)	37.6	68.2
5-Max. $\mu m^3/cm^3$	493	6.3 (22.7)	8.9 (43.2)	18.2 (58.9)	40.0	72.0
0-5 $\mu m^3/cm^3$	126	2.3 (64.0)	3.2 (106.4)	5.9 (169.4)	28.6	53.2
5-10 $\mu m^3/cm^3$	132	0.7 (10.0)	3.6 (50.0)	4.3 (59.4)	27.3	59.8
10-20 $\mu m^3/cm^3$	184	3.1 (19.8)	5.9 (39.9)	8.1 (53.1)	45.1	75.0
20-30 $\mu m^3/cm^3$	97	8.8 (36.4)	9.9 (40.7)	16.7 (63.4)	45.4	80.4
30-50 $\mu m^3/cm^3$	58	11.2 (28.5)	15.1 (39.5)	25.6 (65.7)	55.2	79.3
50-100 $\mu m^3/cm^3$	18	27.1 (46.1)	29.0 (49.2)	24.1 (42.9)	11.1	66.7
100-Max. $\mu m^3/cm^3$	4	116.7 (60.1)	116.7 (60.1)	58.6 (33.9)	0.0	50.0